Title
Mapping the phase diagram of alkyl ligands on nanoparticle surfaces with molecular simulations and field theoretic models

Author
Satish, Pratima

Publication Date
2019

Peer reviewed|Thesis/dissertation

Mapping the phase diagram of alkyl ligands on nanoparticle surfaces with molecular simulations and field theoretic models

by

Pratima Satish

A dissertation submitted in partial satisfaction of the

requirements for the degree of

Doctor of Philosophy

in

Chemistry

in the

Graduate Division

of the

University of California, Berkeley

Committee in charge:

Professor Phillip Lewis Geissler, Chair
Professor Eran Rabani
Professor Jeff Neaton

Fall 2019

Mapping the phase diagram of alkyl ligands on nanoparticle surfaces with molecular simulations and field theoretic models

Abstract

Mapping the phase diagram of alkyl ligands on nanoparticle surfaces with molecular simulations and field theoretic models

by

Pratima Satish

Doctor of Philosophy in Chemistry

University of California, Berkeley

Professor Phillip Lewis Geissler, Chair

Some of the most important and interesting phenomena in physical chemistry, such as heterogeneous catalysis, semi-conduction, and self-assembly depend crucially upon the surface properties of the material under consideration. This is particularly relevant for nanoscopic objects, whose surface-to-volume ratio is much higher than macroscopic materials. Thus, it is often necessary to carefully engineer nanoparticle surfaces so as to prevent them rom coalescing or reacting with their environment. This is achieved by using passivating ligands that stabilize nanoparticle surfaces and consequently, modify the chemical, optical, and electrical properties of nanocrystals and modulate inter-nanoparticle interactions. As a result, gaining an understanding of ligand behavior is essential to synthesizing new nanomaterials with useful technological applications; particularly because probing ligand structure is experimentally difficult.

We approach this problem by performing atomistic computer simulations of alkyl ligands on a semiconducting nanocrystal facet to elucidate their phase behavior at different temperatures and solvent conditions. These simulations provide a detailed description of the structure of the ligand molecules, specifically providing insight into the order-disorder transition they undergo as the temperature is varied. This phase transition changes the arrangement of the surface ligands, affecting how a nanoparticle interacts with solvent and other nanoscale objects in its environment. We proceed to map the observed statistics of ligand orientation onto a coarse-grained field theoretic model of the ordering transition, which is parametrized by physical properties obtained from simulation data. By extracting the underlying physics of the transition and removing irrelevant atomistic details, this coarse-grained model considerably reduces computational costs, while still describing the collective behavior of ligand molecules on a nanoparticle surface. This new understanding can be leveraged to describe ligand ordering when multiple nanoparticle surfaces are close to each other and its effect on the phase behavior of ligand passivated nanocrystals.

To loved ones, near and far.

Contents

List of Figures

List of Tables

Acknowledgments

These past five and a half years would have been very difficult without the support and encouragement of some of the people I met at Berkeley. I grew a lot, becoming physically, mentally and emotionally stronger, learning to think inward and finding my own power.

I want to thank my advisor, Phill Geissler, for making me an independent scientist, so that I could learn how to communicate my research interests effectively and solve challenging problems on my own. As a member of his research group, I decided how to proceed in my graduate career, focused on connecting the bigger picture with the smaller details and forged meaningful connections with other researchers.

The most important of those people were John Haberstroh, Jaffar Hasnain and Katie Klymko. John – since the moment you helped me calm down before taking my driving test, you've been there as a source of immense scientific knowledge and support. Jaffar – thank you for listening to all my rants, big and small, keeping it warm in our office space, and helping me with everything, especially in the last couple years. Katie – our gym, food and science bonding sessions have been so great for me to relax and reconfigure; thank you for your enthusiasm in my research and also allowing me to feed you constantly, deepening my passion for sharing meals with people I love.

I could not have done it without the administrative folks who basically figured out how to help me survive and get paid - the late Lisa Littlejohn (thanks for shouting at the DMV), Leslie Detterick (thanks for the constant snacks and laughs), Natalie Johnson (thanks for printing crazy amounts of discussion sheets) and Sara Russell (thanks for being so accommodating with last minute requests).

Others who helped me at different points just by listening and providing advice when needed – Katie Deeg, Georg Menzl, Cory Hargus, Jeremy Nowak, Steve Cox, Andreana Rosnik and anyone else I forget – thank you for reaching out whenever you did.

To my RSF community which helped me deal with the stress of grad school by providing a constant way to stay healthy – I cannot emphasize how much this changed my life for the better. The various group ex coordinators (Danielle, Andra and Sue), gym teachers whose classes I looked forward to at the beginning/end of my workdays (Geoffrey, Robbie, Shola, Anne, Devin, Miwa, Shane and others), and especially my Urbankick class attendees who made teaching cardio kickboxing amazing every Monday and Tuesday nights – they were all a huge part of keeping me sane these past few years.

In a similar way, taking three years of Polish classes has left a lifelong impact. I can now adequately communicate with new family members, and most importantly, impress any Polish person I meet by saying "hello". Thanks to Katarzyna Zacha for patiently teaching me all those years and a rotating cast of students conversations and discussions with whom helped me improve my speaking skills.

My dearest friends at Berkeley and beyond – Tom Osborn Popp (and his great dad!), Steven Lyle, Chris Kaplan, Katie Klymko (our witness!), Stefan Fischer, Justin Ondry, Ashwathi Iyer, Lucjan Żołnierowski, Vasudha Deshpande, Jaffar Hasnain and Sam Hagerbaumer, amongst many others – your support, emotional and scientific, has been one of the brightest

spots in my time here. It made the hugest difference, especially compared to my time at Cornell, and feeling loved by so many people... my gratitude cannot be expressed in words.

My family, who sent their constant love and support from Bombay, Northfield, MN and now, Warszawa – thank you for being there, through good times and bad and never questioning my ability to keep at it. You expressed enthusiasm when I was excited, found positivity when I felt down about something and commiserated when I felt treated unfairly. And on a whole other note, both my families are throwing two weddings to celebrate and share my joy, and I cannot be more thankful for and appreciative of all their efforts and hard work to do all of it while I focused on wrapping up my dissertation. Again, how I feel is indescribable – I just hope I express my feelings appropriately.

Last but definitely not least, I want to thank my best friend, husband and partner (those words in no particular order), Wojtek Osowiecki, most of all for being there through everything. I am so lucky to have you, and I wouldn't know what to do without you, especially when it comes to opening cans, tanking cars and paying my taxes. But jokes aside, my life changed thanks to you and I wouldn't have it any other way. Risking being cheesy despite all my claims to the contrary, bardzo Ciebie kocham!

Chapter 1

Introduction to nanoparticles: surface structure and related properties

Nanoparticles are particles with dimensions of $10^{-7} - 10^{-9}$ m, unfathomably smaller than everyday objects of size $10^{0} - 10^{2}$ m [1]. Atomic sizes are usually around 10^{-10} m; this means that nanoparticles are closer to atoms in terms of behavior and properties, than they are to bulk materials [32]. This difference of magnitude changes the structure and properties of nanoparticles immensely because nanoparticles have a much higher surface-to-volume ratio as compared to bulk materials. The contribution from surface regions, which is overwhelmed by bulk behavior for macroscopic objects, is much more significant at the nanoscale, giving nanoparticles mechanical, optical, chemical, and electronic properties distinct from macroscopic bulk materials , [32, 46, 16, 36]. Fig. 1.1 shows a transmission electron microscopy (TEM) image of rod-shaped nanoparticles made of cadmium sulfide (CdS) [2], with a scale bar showing the size of these nanorods.

The ability to atomically resolve the structure of nanoparticles means that one has the ability to tune properties by controlling the morphology [52]. In particular, the higher surface-to-volume ratio of nanoparticles is key to understanding their difference as compared to macroscopic materials. Synthesizing particles with controlled shape and surface structure can help manipulate inter-nanoparticle interactions as well as the properties of nanomaterials [1]. Hence, elucidating the structure of and phenomena occurring at a nanosurface is very important to understand nanoparticle properties, which makes them good candidates for various technological applications [2, 47, 40, 30, 20].

1.1 Nanoparticle structure and surface chemistry

Nanoparticles can have underlying different crystal structures depending on their composition. Hence, the surfaces of these particles can belong to different families of crystallographic facets. Semiconductor nanoparticles, with applications in optics and electronics, are usually made from II-VI precursors and have the wurtzite crystal structure [35, 36]. A TEM image

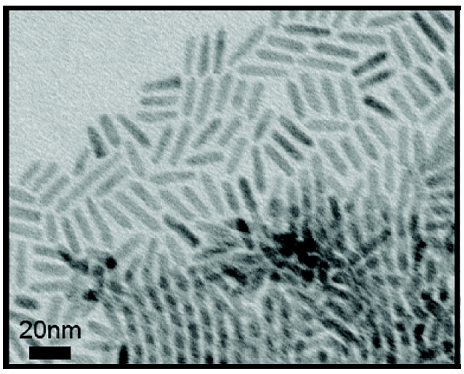

Figure 1.1: A TEM image of rod-shaped CdS nanoparticles. The scale bar at the bottom left shows the typical size of these nanoparticles. Reprinted (adapted) with permission from [2]. Copyright (2009) American Chemical Society.

of a CdS nanosphere, which has the wurtzite crystal structure, showing atomic resolution as well as different facets, is shown in Fig. 1.2.

These nanoparticle surfaces are functionalized by organic molecules, known as ligands, attached to their surfaces. These molecules passivate the surface, stabilizing the particles at the nanoscale [8]. They also affect the physical and chemical properties of nanoparticles [51], enhance solubility in different solvents and mediate inter-particle interactions [10, 48]. Therefore, in addition to the choice of different II-IV semiconductors and nanoparticle faceting, the composition, length, and grafting density of ligands become additional factors that can be manipulated to produce desired nanomaterial properties [49, 32, 42, 21].

In conclusion, experimental validation of ligand behavior is difficult [22], especially since there are many different parameters that can be tuned. Hence, even though there is tremendous potential for ligands to be used as tools to make new materials [34, 19], gaining microscopic insight in the laboratory is very difficult and usually indirect [3]. There is a need for a different approach to understand the structure and dynamics of ligand molecules attached to nanoparticle surfaces.

1.2 Computer simulations of ligands on nanoparticle surfaces

We used computational techniques and statistical mechanics in order to elucidate ligand behavior on nanoparticles. Computer simulations and theories on self assembly are indispensable in the rational design of functional nanomaterials because they uncover relevant energies, length scales, and trends hidden in the large number of variable parameters available to synthetic chemists. In addition to sampling a large parameter spaces, molecular dynamics

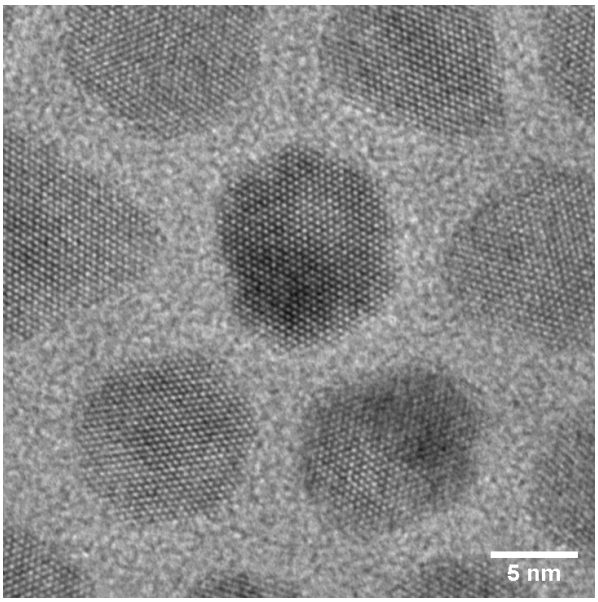

Figure 1.2: A TEM image of CdS nanoparticles, showing atomic scale detail. The surfaces of different particles are faceted, which belong to different crystallographic lattice planes of the wurtzite crystal structure. Image courtesy of Justin C. Ondry.

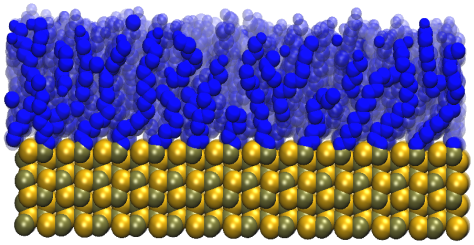

Figure 1.3: A snapshot of ligand molecules attached to a CdS(100) surface, taken from a MD computer simulation. The blue ligand molecules attach to brown Cd atoms, which form a crystal lattice with the yellow S atoms.

(MD) simulations provide insights at the molecular level, that are difficult to obtain from in situ experiments. A snapshot from an MD simulation of ligand molecules attached to a CdS nanosurface is shown in Fig. 1.3.

The major challenge in simulating such systems is that they consist of many molecular degrees of freedom. Especially as one scales up from one nanosurface covered with hundreds of ligands to multiple nanoparticles with ligands attached to different crsytalline facets, MD

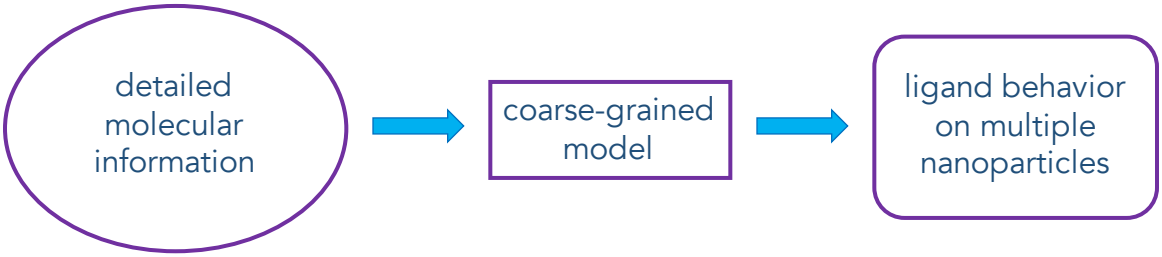

Figure 1.4: A schematic showing the workflow used to understand ligand behavior on nanoparticle surfaces. Using MD simulations and a field theoretic model, a better understanding of ligand molecules and how they affect inter-nanoparticle interactions can be developed.

simulations become very computationally expensive. Fortunately, the field of statistical mechanics is well equipped to circumvent the difficulty of simulating many-body systems. We perform tractable MD simulations of ligand molecules on a CdS surface, and then develop a coarse-grained field theoretic model that helps us understand which nanoscopic degrees of freedom are the most important. We take inspiration from Landau-Ginzburg theory, which postulates a phenomenological model of superconductors [18, 13], to describe a model of ligand molecules on nanoparticle surfaces. This allows us to collapse all the atomic and molecular details into a few degrees of freedom that dictate ligand behavior at the macroscopic scale.

The ultimate goal of this work is to extract intuitive quantities from our large-scale molecular simulation data that describe our transition in a coarse-grained model. This simple model can eventually be used to describe the ligand interactions between facets belonging to different nanoparticles, as shown in the schematic in Fig.1.4. This strategy has been applied to predict the phase diagram of water in different conditions [27, 26] and the ordering of phospholipid bilayers [9, 31]; we want to develop a similar theory of nanoparticles coated with ligand molecules.

1.3 Ligand properties and behavior in solution

Taking a closer look at the ligand molecules, one finds that they are usually attached to the nanoparticle via a charged head-group that attaches to a dangling bond on the surface. The structure of a typical ligand, octadecylphosphonic acid, is shown in Fig. 1.5. This ligand attached to Cd atoms on the surface via an ionic bond. Nanoparticle facets belonging to different lattice plane families have different numbers of interfacial Cd atoms, leading to variation in the density of ligand molecules on different surfaces. We study the behavior of octadecyl phosphonate ligands attached to a Cd(100) facet, which has two crystallographically distinct dimensions.

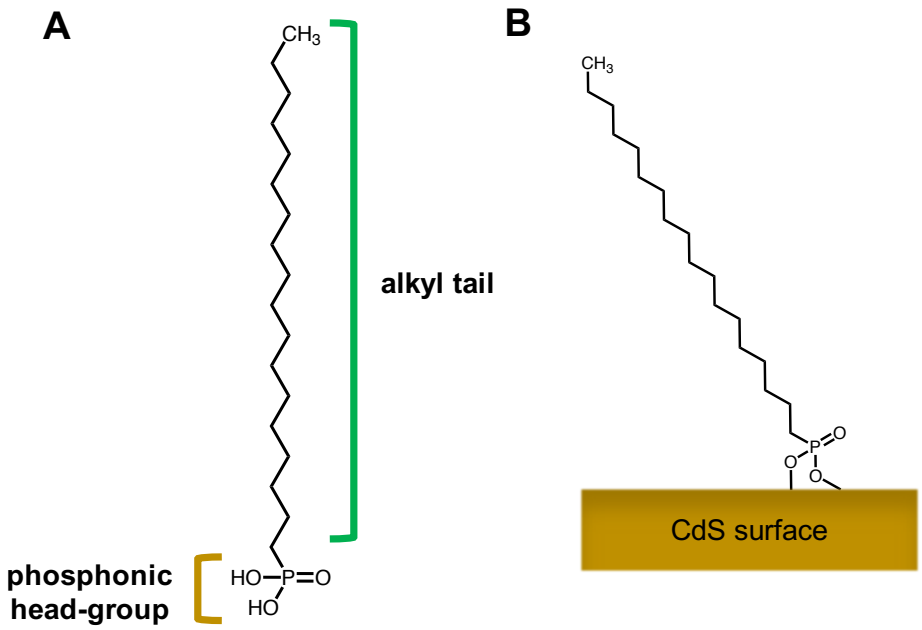

Figure 1.5: A) Structure of the octadecylphosphonate ligand, a molecule typically used to passivate wurtzite nanoparticle surfaces. B) The phosphonic acid head-group loses hydrogen to form a charged phosphonate entity, that can ionically bond with Cd atoms to passivate the nanosurface.

These ligands can also self-assemble on the nanosurface under appropriate conditions, forming self-assembled monolayers. These packed ligand bundles have been observed in MD simulations previously [12, 42, 48, 49] and Fig. 1.6 shows how alkanethiol ligands pack on gold (Au) nanospheres at different temperatures. The curvature of the nanoparticle affects the packing of the ligands; at lower temperatures, packets of ligands order along different directions due to the underlying geometry. Hence, the facets of the nanoparticles affect the self-assembly behavior of the ligand molecules [12, 49].

As a result of passivating at the nanoscale, ligands form different phases and understanding the structure of these phases is essential to understanding molecular properties [3]. Fig. 1.7 shows the ordering of octadecyl phosphonate ligands on the CdS(100) facet. This is the same system as shown in Fig. 1.3, just at different conditions that cause the ligands to align along a given direction. The self-assembly of ligands into an ordered state is a phase transition that changes the surface structure of a nanocrystal, and can potentially change inter-nanoparticle interactions [48, 50].

In this way, ligand self-assembly can be a driving force for nanoparticle self-assembly [32, 23]. The direction of ligand packing in an ordered phase can change interactions between nanoparticles [17], REF- Asaph. This is shown schematically in Fig. 1.8, where the ordering

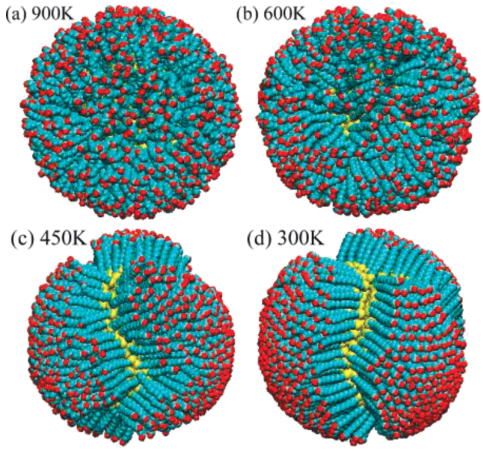

Figure 1.6: (a)-(d) Snapshots from MD simulations of alkanethiol ligands attached to a Au nanoparticle at different temperatures. As the system cools down, the ligands start ordering along specific directions. The shape and curvature of the nanoparticle surface leads to the formation of several bundles. Reprinted (adapted) with permission from [12]. Copyright (2007) American Chemical Society.

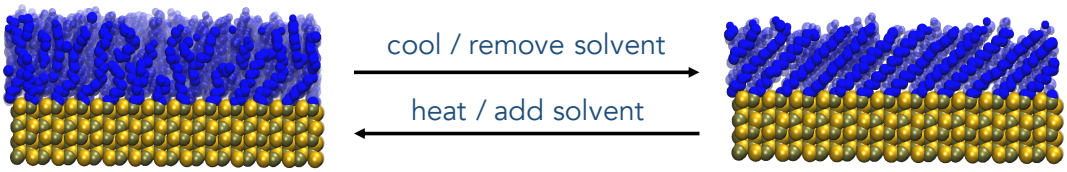

Figure 1.7: Ligand ordering on a CdS facet, which occurs as a result of changing the temperature or solvent. The ligands orient along a specific direction, self-assembling into an ordered phase.

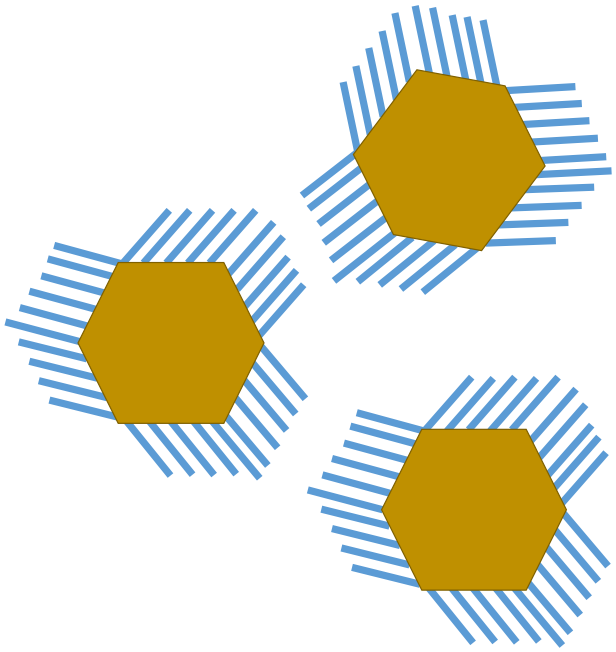

Figure 1.8: Schematic showing how ordered ligands on nanoparticle facets can affect the interactions between different nanoparticles. Since the ordered ligand bundles point along a given directions, the angles of approach by another nanoparticle are restricted. This can play a role in the spatial packing of nanocrystals, leading to large-scale nanoparticle self-assembly.

of ligand molecules can give rise to packing of other nanoparticles along certain directions. Experimental results showing self-assembled nanoparticle superlattices are shown in Fig. 1.9 but the forces leading to these structures are not fully understood. Using ligands to control and tune the self-assembly of large arrays on nanoparticles [11, 29] is a potential way to synthesize new nanomaterials with desired structure and properties [38, 5].

The ligand self-assembly from an ordered to a disordered phase is a first-order phase transition. The ligands used to passivate nanoparticles usually have melting temperatures around 273-373K [43, 25]. On a nanoparticle facet, this transition temperature can be controlled by changing the surface coverage or chain length of ligands, which can bring the disordering transition close to room temperature. Hence, this self-assembly phenomenon can cause nanocrystal superlattices to form at relatively low temperatures.

1.4 Summary

In this thesis, we study and order-to-disorder transition that the ligands attached to nanoparticle surfaces undergo. The details of molecular dynamics simulations of the ligand ordering phenomenon are described in Chapter 2. Chapter 3 covers the development of a coarse-

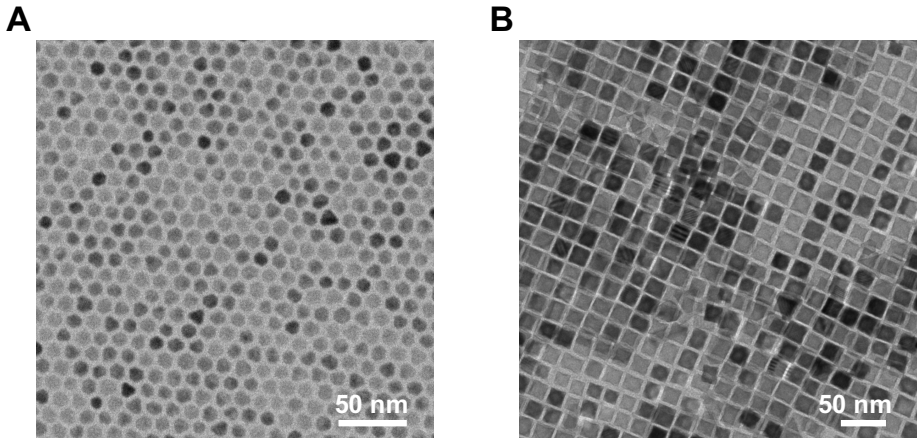

Figure 1.9: A) TEM image of CdS nanoparticles self-assembled in a hexagonal close-packed structure. B) TEM image of $CoFeO_3$ nanoparticles which form a superlattice with cubic packing. Images courtesy of Justin C. Ondry.

grained field theory representing this phase transition. In Chapter 4, the data from the MD simulations is used along with the coarse-grained model to parameterize the interactions between octadecyl ligands in vacuum as well as hexane, a commonly used solvent. The field theoretic model presented here can be used to represent ligand behavior on a single nanoparticle surface, as well as extend it to multiple facets covered with ligands, as shown in Fig. 1.8, to start building a model of ligand-nanoparticle interactions.

Chapter 2

Molecular dynamics simulations of ligands on CdS surfaces

Our motivating goal is to understand how alkyl phosphonate ligands behave on semiconducting nanoparticles and how they affect inter-nanoparticle interactions. These ligands can order and disorder given appropriate conditions, a transition that can be straightforwardly examined by MD simulations at the single-nanoparticle scale. However, a large collection of nanoparticles is computationally expensive to simulate thoroughly in atomistic detail. Our approach is to use information from MD simulations of a single extended ligand film to construct a field theory that can be adapted to describe ordering in larger and more complicated systems. Thermodynamic characterization of the ligand ordering transition enabled by these simulations is further useful in elucidating how ligand interactions play out on the microscopic scale and change inter-nanoparticle forces.

2.1 System setup to study ligands on CdS surface

Self-assembled monolayers (SAMs) occur both in the presence of solvent and in its absence. We studied both scenarios for octadecyl carbon chain ligands (C_{18}) attached to a CdS surface, in order to understand the contribution from ligand-ligand interactions as well as the influence of solvent. In both cases we a periodically replicated 8.1×8.2 nm slab of CdS. The arrangement of atoms in this slab follows the wurtzite crystal structure adopted by CdS nanoparticles [36, 35], with lattice constants $a_x = 4.12$ nm and $a_z = 6.75$ nm. The surface to which ligands are bound is a (100) facet, so that the surface normal points along the y-direction and the facet is parallel to the $xz-$plane. For the wurtzite crystal structure, the (100) facet has the maximum number of exposed Cd atoms [49, 41]. The C_{18} ligands attach to this crystal facet via their negatively charged phosphonate head groups which form an ionic bond with Cd atoms. Experimentally a wide variety of surface coverage has been observed [50, 49]. For simplicity, we take all the possible sites to be passivated (i.e., 100% passivation), avoiding ambiguity in choosing which sites are occupied and, importantly for

our purposes, preserving translational symmetry. The field theory we develop for this case of maximum passivation should serve as a useful starting point for lower levels of passivation.

2.2 Dynamics used for MD simulation propagation

Large-scale Atomic/Molecular Massively Parallel Simulator (LAMMPS) was used to perform MD simulations. Ligands were simulated at fixed volume and temperature, for which a Nosé-Hoover thermostat was used. The cadmium and sulfur atoms were fixed in place in order to reduce computational costs, as their vibration does not significantly affect the ligand ordering phenomenon. This was done by excluding them from the thermostat. A Störmer-Verlet time integrators with a 1 fs time-step was used, and equilibration runs were 5 ns long. The production runs used to calculate average quantities were also 5 ns long, unless noted otherwise.

2.3 Ligand force fields for performing MD simulations

The ligand ordering of interest shares many basic features with bulk crystallization. A force field that accurately captures physical properties across phase transitions is therefore essential. We specifically study a united-atom potential parameterized to accurately represent thermophysical properties of alkyl chains in different phases. This potential models each CH_x group in the ligand molecule as one unit. These pseudo-atoms interact with each other via dispersion forces and volume exclusion, described using Lennard-Jones potentials. Pseudo-atoms in the same molecule interact with each other through bonding, bending and dihedral potentials. The force field parameters for these interactions were taken from Transferable Potentials for Phase Equilibria (TraPPE) [28, 33], extended to include bond stretching in order to ensure compatibility with LAMMPS [37]. The different ligand interactions include the following terms:

$$U_{\mathrm{NB}}(r_{ij}) = 4\epsilon_{ij}\Big[\Big(\frac{\sigma_{ij}}{r_{ij}}\Big)^{12} - \Big(\frac{\sigma_{ij}}{r_{ij}}\Big)^{6}\Big]$$

$$U_{\mathrm{bond}}(r) = \frac{k_{\mathrm{bond}}}{2}(r - r_0)^2$$

$$U_{\mathrm{angle}}(\theta) = \frac{k_\theta}{2}(\theta - \theta_0)^2$$

$$U_{\mathrm{dihedral}}(\psi) = c_0 + c_1[1 + \cos(\psi)] + c_2[1 - \cos(2\psi)] + c_3[1 + \cos(3\psi)]$$

In the above equations, ϵ_{ij} and σ_{ij} are Lennard-Jones energies and diameters, respectively, and follow the usual Lorentz-Berthelot rules for obtaining interactions between different atomic types. k_{bond} is the spring constant for the bonding potential at an equilibrium bond length r_0 and similarly, k_θ is the bending spring constant with equilibrium angle θ_0. The sets of constants $\{c_i\}$ parameterize the torsion potential of the alkyl chains.

Type	ϵ (kcal/mol)	σ (Å)
$[CH_3]$-CH_x	0.195	3.75
$[CH_3]$-Cd,S	0.143	3.54
$[CH_2]$-CH_x	0.0914	3.95
$[CH_2]$-Cd,S	0.111	3.54

Table 2.1: Non-bonded interaction parameters used for MD simulations of octadecyl molecules on a CdS(100) surface.

Type	k_{bond} (kcal/mol-Å^2)	r_0 (Å)
$[CH_x]$-CH_y,Cd	95.9	1.54

Table 2.2: Bonding potential parameters used for MD simulations of octadecyl molecules on a CdS(100) surface.

Type	k_{angle} (kcal/mol-rad^2)	θ_0 (rad)
CH_x-$[CH_2]$-CH_y	62.1	1.99

Table 2.3: Bending potential parameters for MD simulations of octadecyl molecules on a CdS(100) surface.

The CdS-CH_x non-bonded interactions were adapted from a Lennard-Jones potential, previously designed for Au atoms, but modified to reflect the Hamaker constant and density of CdS [39, 7]. Ligands' phosphonate head groups, whose strong bonds to Cd offer little range of motion, were not explicitly represented in the simulation. They are in effect subsumed into the surface Cd atom. The last pseudo-atom in every octadecyl chain therefore is attached to a surface Cd atom with the same potential that describes intra-molecular bonds. The values used for all the MD simulation force field parameters are shown in Tables 2.1-2.4.

Type	c_0 (kcal/mol)	c_1 (kcal/mol)	c_2 (kcal/mol)	c_3 (kcal/mol)
CH_x-$[CH_2$-$CH_2]$-CH_y	0.0	1.4114	-0.2711	3.1458

Table 2.4: Dihedral torsion parameters for MD simulations of octadecyl molecules on a CdS(100) surface.

2.4 Structural details of ligand arrangement in ordered phase

When ligands order, their net orientation points at an angle to the surface normal vector (i.e., the y-axis). We therefore focus on the yz-component of orientational fluctuations, which most directly distinguishes ordered and disordered phases. Our order parameters are specifically based on the projection of each ligand's head-to-tail vector onto the $yz-$plane. The angle between this projection and the $y-$axis we call θ_z, shown in Fig. 2.1. The spatially averaged orientation Θ_z for the whole layer is given by

$$\Theta_z = \sum_i \theta_z(i)/N_{\text{lig}}\,,$$

where $\theta_z(r_i)$ refers to the orientation angle of ligand i on the surface. Our primary order parameter $\langle\theta_z\rangle$ is defined as the time average of Θ_z over the course of a simulation,

$$\langle\theta_z\rangle \equiv \sum_t \Theta_z(t)/T\,.$$

In the ordered phase, the probability distribution of Θ_z is centered around the highly negative value of $\langle\theta_z\rangle$. In the disordered phase, $\langle\theta_z\rangle$ has a value closer to zero, but still slightly negative. This remnant asymmetry of the disordered phase arises from the polarity of the underlying wurtzite structure. A schematic of the molecular configurations in the different phases are shown in Fig. 2.1.

Ligand molecules in the ordered phase are organized more intricately than in many SAMs, which complicates our analysis. The wurtzite crystal structure has a two-dimensional rectangular arrangement of Cd sites on the CdS(100) facet, while the densest packing of ligands is achieved in a hexagonal arrangement. In order to accommodate this geometric mismatch, ligand orientation alternates along the $x-$direction, as shown in Fig. 2.2. One row of Cd atoms with the same value of z has ligands with an *anti* C-C bond conformation near the CdS surface; the next row has ligands with a *gauche* conformation; the next row is *anti*, and so on. When viewed from a $\pi/2$ rad angle along the $yz-$plane as in Fig. 2.3, the symmetry change can be seen quite clearly in the ligand configurations. This alternation is quantitatively evident in the probability distribution $P(\theta_z)$. Fig. 2.4A shows this distribution for ligand layers in vacuum (no solvent) at a low temperature representative of the ordered phase, and at a high temperature representative of the disordered phase. The two peaks in the ordered distribution represent the orientation angles for *anti* and *gauche* rows. When the angles are spatially averaged across the CdS facet, the peaks collapse onto the average, showing a narrow distribution about $\langle\theta_z\rangle_{\text{ord}} = -0.74$ rad, as shown in Fig. 2.4B. In the disordered phase, the probability distribution is broader, as more fluctuations are allowed, and it is peaked about $\langle\theta_z\rangle_{\text{disord}} = -0.30$ rad. This complicated structural arrangement causes issues for performing MD simulations.

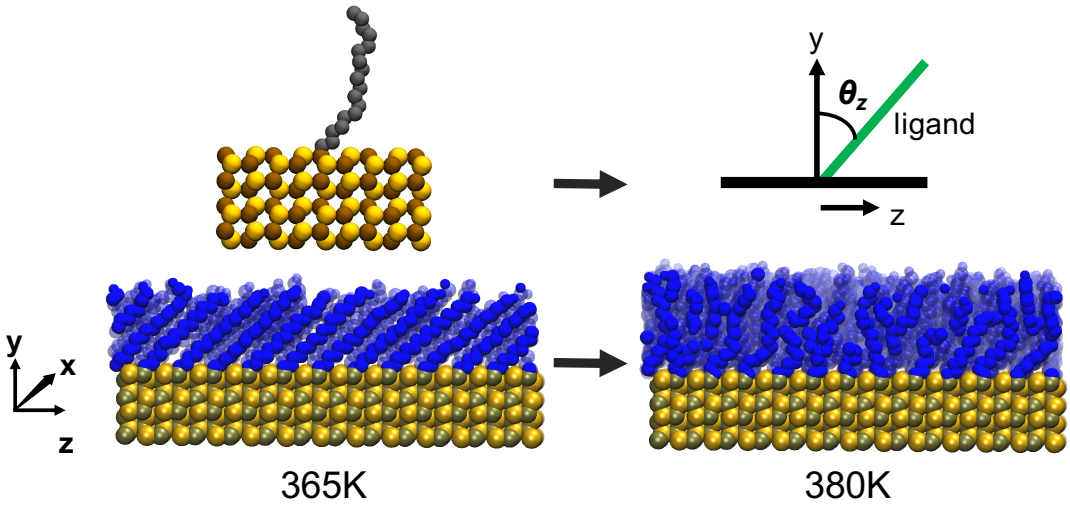

Figure 2.1: A) Configuration of an individual ligand on the CdS surface and its representation as an alignment angle, which is used to calculate the order parameter for the system. B) Snapshots from the MD simulations at two different temperatures showing ligand configurations in the ordered and disordered phases. The coordinate system for the simulations is depicted in the axes shown on the left.

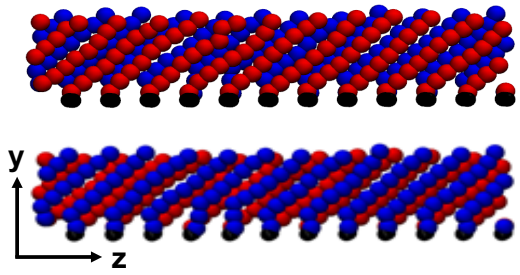

Figure 2.2: Ligand arrangement in the ordered phases, forming rows with alternating bottom C-C bond conformations. This allows the ligands to adapt the symmetry in the ordered phase and change from the rectangular CdS facet to a hexagonal lattice.

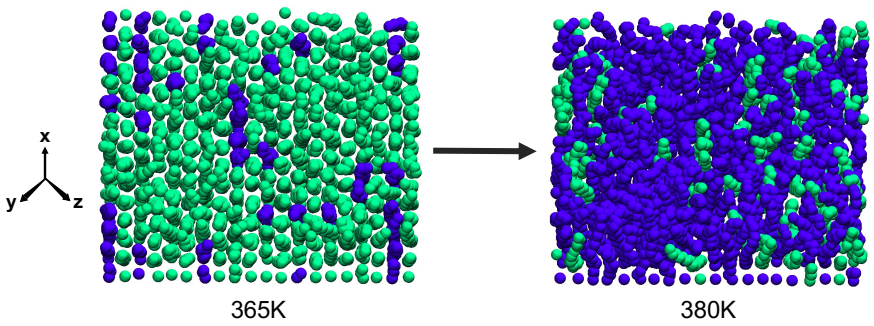

Figure 2.3: When viewed at a 45° in the $yz-$plane, the hexagonal packing structure of the ligands in the ordered phase is clearly visible. This structural motif seems to disappear in the disordered phase.

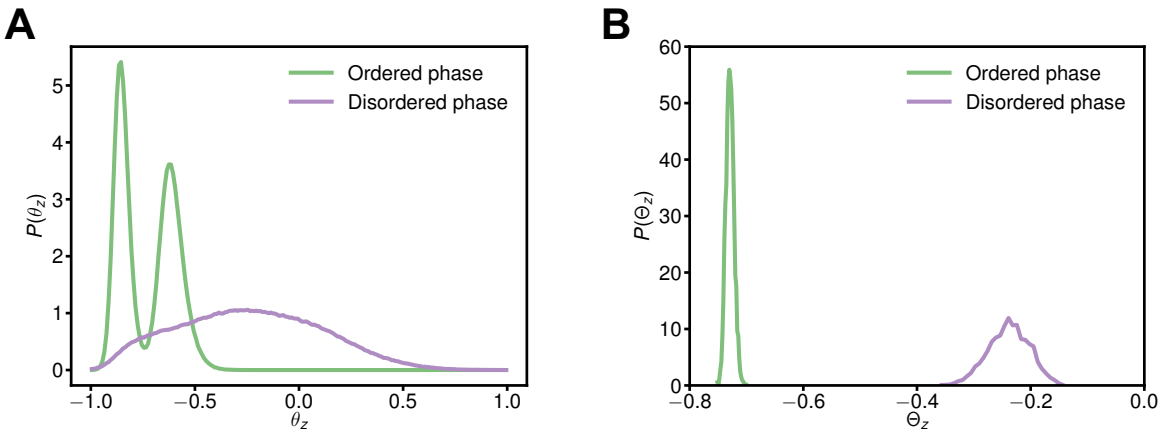

Figure 2.4: A) Probability distribution of θ_z in the ordered and disordered phases in vacuum. B) The same distributions, but this time for Θ_z.

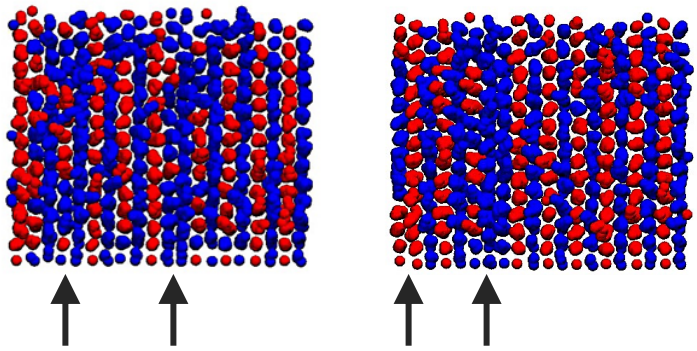

Figure 2.5: Snapshots from MD simulations showing defects in ligand alignment obtained upon cooling from the disordered phase. The arrows show areas of disorder, emerging either as patches, in the left image, or as double *anti* or *gauche* rows, shown in the right image.

2.5 Equilibration and sampling issues with straight molecular dynamics

Due to the coherent alternation of ligand conformations in the ordered phase, reversible transformations between ordered and disordered phases are difficult to achieve in straightforward MD simulations. For example, an initial configuration representative of the disordered phase, evolved at low temperature over tens of nanoseconds, almost invariably produces a structure that is locally ordered but globally defective. Fig. 2.5 shows examples of such incompletely annealed configurations, one exhibiting patches of disorder and the other a pair of defects in the *anti-gauche* alternation pattern. These imperfections are dynamic at temperatures modestly below the ordering transition, migrating across the surface during the course of a simulation, but they do not heal. In this sense they are kinetically trapped over accessible time scales, and therefore greatly hinder statistical sampling. This issue presents a general challenge for confidently surveying structural fluctuations in the temperature range of interest. It is especially problematic for assessing the relative stabilities of ordered and disordered phases (and therefore for locating the transition between them). Unless trajectories can repeatedly create and anneal pertinent defects, the statistical weights of the two phases cannot be quantitatively compared. We explored several methods for addressing this problem, so that facile equilibrium sampling of ordered and disordered states could be ensured.

In order to obtain properly equilibrated ligand configurations, we developed an importance-sampling based approach that gives access to the free energy landscape of the ligands in the space of the chosen order parameter $\langle\theta_z\rangle$. Our chosen solution, biased replica exchange, combines aspects of methods generally used to perform accelerated equilibration, umbrella sampling and parallel tempering. These methodologies are explained below.

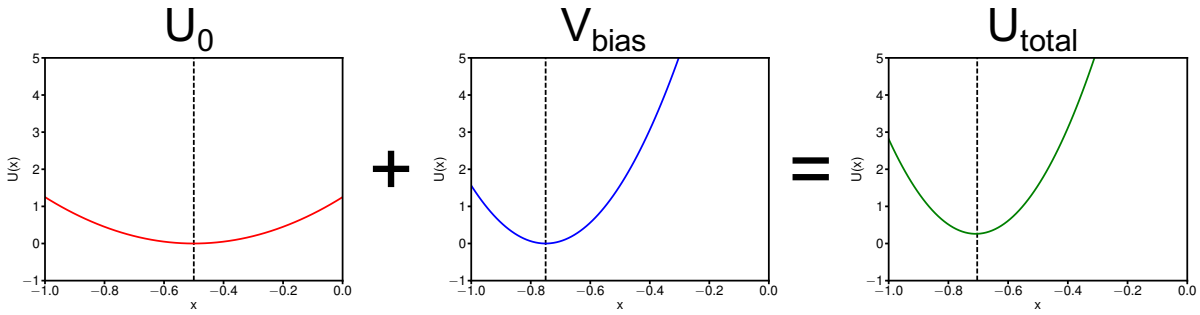

Figure 2.6: The left-most panel represents the underlying potential energy and the middle panel, showing the biasing potential, is added to it. This results in a new landscape being sampled, shown in the right-most panel, with the most probable value shifting to the left due to the addition of V_{bias}.

2.6 Development of biased replica exchange to explore system behavior

Umbrella sampling involves introducing a biasing potential to modify the statistical weight of regions of phase space that have barriers or high free energy. This bias modifies the potential energy landscape and enhances sampling in the areas that are generally inaccessible in a straightforward MD simulation. For a given configuration r^N with underlying potential energy $U_0(r^N)$, the biasing potential $V_{\text{bias}}(r^N)$ re-weights the equilibrium probability according to,

$$\begin{aligned} U_{\text{total}}(r^N) &= U_0(r^N) + V_{\text{bias}}(r^N) \\ \implies P_{\text{bias}}(r^N) &\propto e^{-\beta U_0(r^N)} e^{-\beta V_{\text{bias}}(r^N)} \end{aligned} \tag{2.1}$$

We are specifically interested in biasing fluctuations in ligand orientation as described by the order parameter Θ_z. Our bias potential thus depends on configuration r^N through its associated value of $\Theta_z(r^N)$. With the form of a Hookean spring, $V_{\text{bias}}(r^N) = \frac{k_{\text{bias}}}{2}\left(\Theta_z(r^N) - \bar{\theta}\right)^2$ favors values of Θ_z near $\bar{\theta}$ where the potential is minimized. The parameter k_{bias} sets the stiffness of the spring. As a result, the overall probability distribution of Θ_z is shifted closer to $\bar{\theta}$, improving sampling in regions away from the thermal averages $\langle\theta_z\rangle_{\text{ord}}$ and $\langle\theta_z\rangle_{\text{disord}}$ characteristic of ordered and disordered phases. A pictorial depiction of umbrella sampling with a spring biasing potential is shown in Fig. 2.6. The PLUgin for MolEcular Dynamics (PLUMED) [6], a code which interfaces with LAMMPS to provide functionality to do enhanced sampling, was used to perform MD simulations with spring biasing potentials.

Parallel tempering, also known as replica exchange, is another approach to improve sampling issues and remove kinetic traps in MD simulations. It involves running simultaneous simulations of the system, each known as a replica, at different temperatures and attempting

exchanges of configurations at different temperatures. These exchanges are accepted with a probability based on the Metropolis-Hastings criterion. The probability of finding the system in configuration r_i^N at inverse temperature β_i (temperature T_i) is given by its Boltzmann weight, $p \propto e^{-\beta_i E(r_i^N)}$. If this configuration were associated with a different temperature T_j, its probability would instead be $p_{i\to j} \propto e^{-\beta_j E(r_i^N)}$. Accounting for these Boltzmann factors for both configurations involved in a parallel tempering exchange move yields an acceptance probability,

$$\begin{aligned} p_{\text{accept}} &= \min\left(1, \frac{\exp\big(-\beta_j E(r_i^N) - \beta_i E(r_j^N)\big)}{\exp\big(-\beta_i E(r_i^N) - \beta_j E(r_j^N)\big)}\right) \\ &= \min\Big(1, \exp\big((\beta_i - \beta_j)(E(r_i^N) - E(r_j^N))\big)\Big) \end{aligned} \tag{2.2}$$

This technique, available as the "temper" command in LAMMPS, mimics continuous heating and cooling cycles, not unlike multiple evaporation and condensation events. It should help to facilitate the dissolution of defects and nucleation of a proper ordered phase. Its effectiveness depends on the height of energy barriers that define kinetic traps, and also on the importance of entropic contributions (which are insensitive to changes in temperature). If energetic barriers are large, then a broad range of temperatures must be employed. Otherwise, one phase will not spontaneously nucleate within the other, and replicas will be unable to anneal defects during the course of the MD simulation. Because acceptance rates for parallel tempering decrease exponentially [15] as the difference between the replica's temperatures increases, using a broad range of temperatures presents significant practical challenges.

We find that these two methods – umbrella sampling and replica exchange – are by themselves insufficient to achieve thorough equilibrium sampling for the ligand system. But an approach that combines their merits can successfully navigate persistent defects states, like those in Fig 2.5. This technique is known as replica exchange umbrella sampling and has been proposed as an enhanced sampling method [45], but not commonly used. It involves simultaneous umbrella sampling simulations, spring biasing potentials centered at different values of the order parameter Θ_z. During the course of the simulation, we occasionally attempt to exchange configurations between different biases. A simple schematic is shown in Fig. 2.7. Temperature is kept constant during these simulations and hence, a replica with configuration r_i^N has the following probability:

$$p \propto \exp\Big[-\beta\Big(U(r_i^N) + \frac{k_{\text{bias}}}{2}(\Theta(r_i^N) - \bar{\theta}_i)^2\Big)\Big].$$

If an attempt is made to switch with another configuration r_j^N with a bias center $\bar{\theta}_j$, the acceptance ratio using the Metropolis-Hastings criterion is,

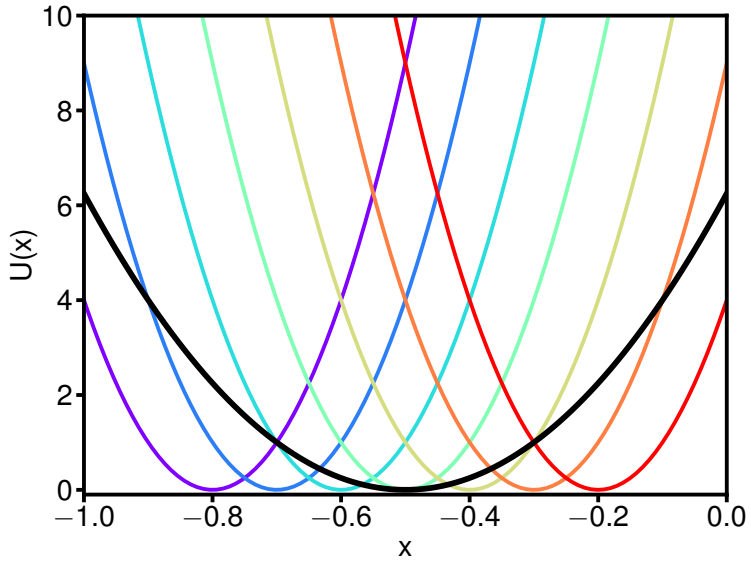

Figure 2.7: The underlying potential energy, shown in black, is sampled by placing several biases along the $x-$axis, shown in varied colors, that are added to the original energy. Equilibration is achieved by attempting exchanges between different biases, allowing proper exploration of the potential landscape.

$$
\begin{aligned}
p_{\text{accept}} &= \min\left(1, \mathcal{P}\right) \\
\mathcal{P} &\equiv \frac{\exp\left[\dfrac{-\beta k_{\text{bias}}}{2}\left[\left(\Theta(r_i^N) - \bar{\theta}_j\right)^2 + \left(\Theta(r_j^N) - \bar{\theta}_i\right)^2\right]\right]}{\exp\left[\dfrac{-\beta k_{\text{bias}}}{2}\left[\left(\Theta(r_i^N) - \bar{\theta}_i\right)^2 + \left(\Theta(r_j^N) - \bar{\theta}_j\right)^2\right]\right]} \\
\implies p_{\text{accept}} &= \min\left[1, \exp\left[\beta k_{\text{bias}}\Big(\Theta(r_i^N) - \Theta(r_j^N)\Big)\Big(\bar{\theta}_j - \bar{\theta}_i\Big)\right]\right]
\end{aligned}
\tag{2.3}
$$

This method is more successful than umbrella sampling or replica exchange individually. As they explore different ranges of Θ_z, ligands are able to anneal out defects and relax fully from their initial state. In particular, we are able to sample a perfectly alternating ordered phase even from configurations that are initially disordered. Biased replica exchange consequently allows determination of relative weights of the ordered and disordered phases, providing access to the underlying free energy surface that the ligands explore.

This functionality, however, does not exist either in LAMMPS or in PLUMED and hence, we wrote a new command in LAMMPS that builds on the PLUMED infrastructure to

combine the parallel tempering and umbrella sampling methods to perform biased replica exchange. We tested the code to ensure acceptance ratios were calculated correctly and were high enough to ensure sufficient exchange between replicas. The new technique was used to thoroughly explore ligand behavior in the $\langle\theta_z\rangle$ phase space at different temperatures, and the results are presented below.

2.7 Resulting ligand configurations and spatial correlations along with subsequent discovery of structure in disordered phase

Standard rendering of ligand configurations in atomistic detail does not provide a strong visual sense for orientational ordering. The alternating *anti-gauche* patterns described above, an important diagnostic for thorough equilibration, are particularly difficult to detect by eye. We have developed two visualization schemes to highlight structural properties of central importance to the ordering transition. In both cases, we assign colors to each ligand according to its orientation θ_z.

One coloring scheme, called **AG**, distinguishes values of θ_z characteristic of an *anti* C-C bond conformation from values typical of a *gauche* C-C bond conformation. Here, any ligand with $\theta_z < -0.78$ rad (corresponding to an *anti* conformation) is colored red. Any ligand with $\theta_z \geq -0.78$ rad is instead colored blue. The latter range includes typical ligands in the ordered phase whose base C-C bond conformation is *gauche*, but it also encompasses orientations that are more typical of the disordered phase. Fig. 2.9 shows representative ordered (A) and disordered (C) configurations visualized in this way. This scheme resolves the fine alternating structure of the ordered phase and thus draws attention to the presence of kinetically trapped defects.

A different coloring scheme, which we call **ODO**, is needed to clearly discriminate regions of the ligand layer that are orientationally ordered from those that are disordered. Here, any ligand with $\theta_z < -0.58$ rad (including all orientations typical of the ordered phase) is colored green. Ligands with $\theta_z \geq -0.58$ rad (including all orientations typical of the disordered phase) are colored purple. Fig. 2.9B and D show ordered and disordered configurations, respectively, visualized with the **ODO** scheme. At low temperatures, this coloring method manifests transient local deviations away from ordered structural motifs. Above the ordering transition, it emphasizes pockets of remnant local order within the disordered phase.

In addition to well-equilibrated ordered and disordered states, biased replica exchange also provides access to intermediate configurations between the two phases. Rendering these configurations with the **AG** and **ODO** coloring schemes, we can track the nucleation and growth of a new phase from the initial state. A series of intermediate configurations associated with Θ_z values between $\langle\theta_z\rangle_{\mathrm{ord}}$ and $\langle\theta_z\rangle_{\mathrm{disord}}$ is displayed in both the coloring schemes in Figs. 2.10 and 2.11. Both sequences show that initial fluctuations in the ordered phase partially disrupt row alignment, and then form a small nucleus of the disordered phase. This

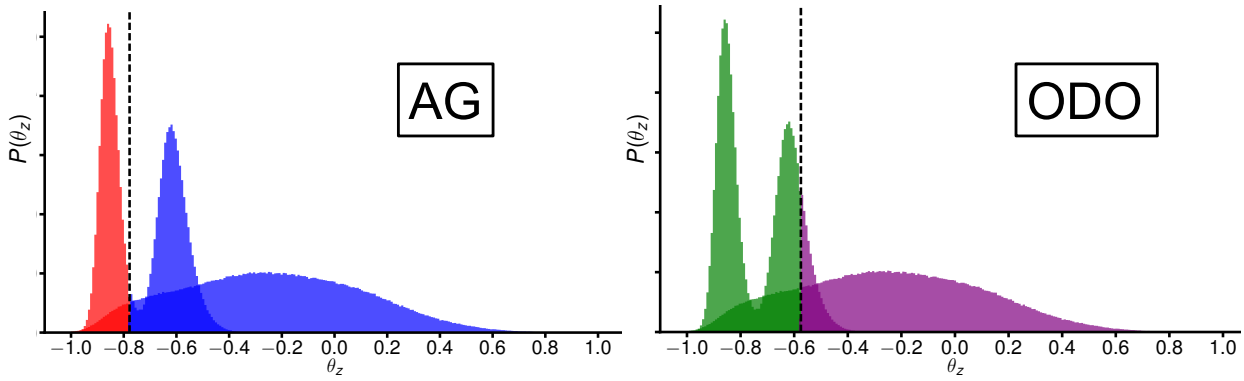

Figure 2.8: Coloring schemes for highlighting different aspects of ligand configuration. The probability distribution for single ligand orientation angle θ_z was used to demarcate between important structural features. The **AG** scheme placed a dividing mark at $\theta_z = -0.78$ rad, shown with a dotted line, and distinguished between *anti* and *gauche* or disordered ligand orientations. The **ODO** scheme showed whether a ligand had a θ_z value that belonged to the ordered or the disordered phase.

nucleus grows to span the system size in the $x-$direction and proceeds to grow along the $z-$axis until all ligands are disordered.

We quantify local deviations from average structure through correlation functions,

$$G_{X_A}\big(|r_1 - r_2|\big) = \Big\langle \big(X(r_1) - \langle X\rangle_A\big)\big(X(r_2) - \langle X\rangle_A\big)\Big\rangle_{|r_1 - r_2|}. \tag{2.4}$$

Here, A labels the phase (ordered or disordered) X is the observable of interest (e.g., the orientation θ_z of an individual ligand), and r_1 and r_2 are two positions on the CdS surface. In writing G_{X_A} as a function solely of the separation vector $r_1 - r_2$, we have exploited translational symmetry of the equilibrium state. We will focus exclusively on pairs of positions that share the same value of x, whose separation distance r is $z_1 - z_2$; or else pairs that share the same value of z, whose separation distance r is $x_1 - x_2$.

Structural features of the ligand phases we have described are reflected in the distance dependence of $G_\theta(r)$. In the ordered phase with perfectly alternating rows in the $x-$direction, $G_{\theta_{\rm ord}}(x)$ tracks the oscillation of Θ_z values in the *anti* and *gauche* rows about $\langle\theta_z\rangle_{\rm ord}$. On the other hand, $G_{\theta_{\rm ord}}(z)$ shows near-perfect correlation as all the ligands in each row have the same θ_z value. These trends are shown in Fig. 2.12. A similar analysis for the disordered phase, Fig. 2.12B, reveals a peculiar feature. Instead of monotonically decaying to zero as r increases, $G_{\theta_{\rm ord}}(x)$ has remnants of the oscillation observed in the ordered phase. The disordered phase thus features spatial patches that not only are more strongly oriented than average but also retain the *anti-gauche* alternation characteristic of the ordered phase.

Remnant structure in the disordered phase is highly robust to heating. Spatial correlation functions computed from 100 ns trajectories at 1000 K are very similar to those determined at

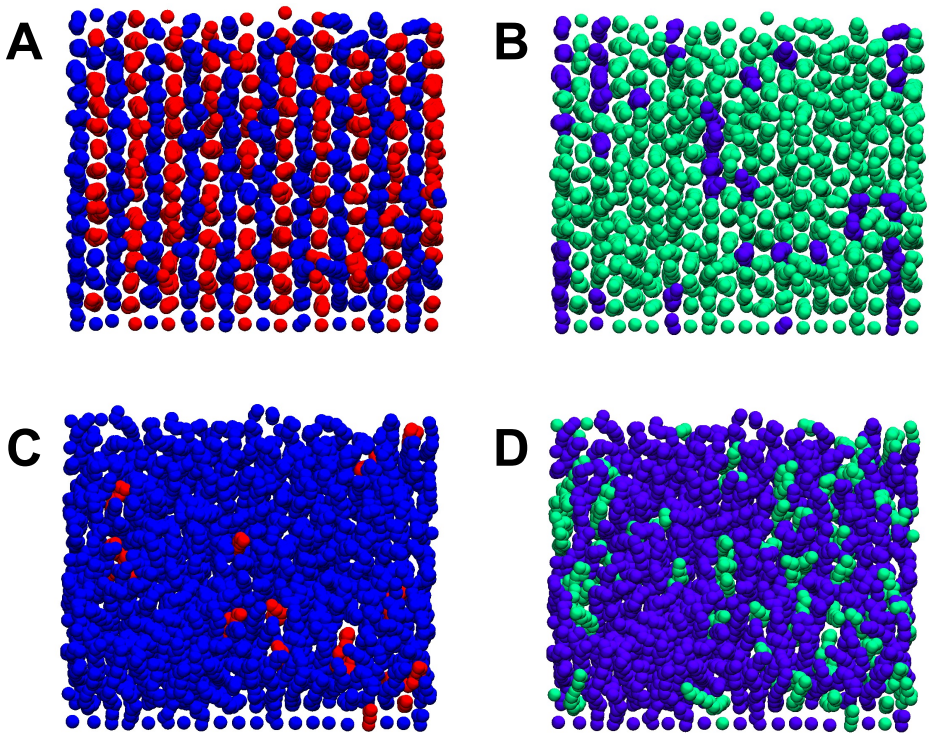

Figure 2.9: Ligand configurations in the ordered phase, colored according to the A) **AG** and B) **ODO** schemes. C, D) The same coloring schemes applied to the disordered phase.

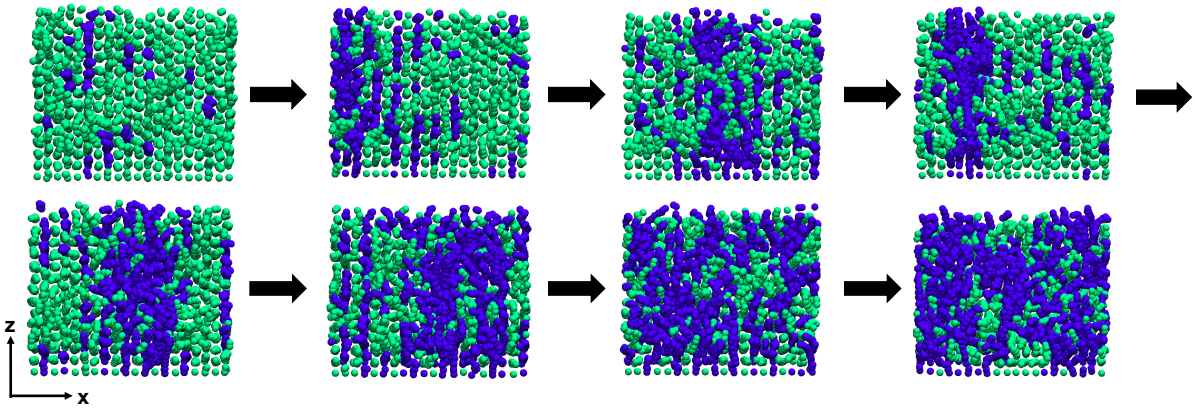

Figure 2.10: A progression of snapshots going from the ordered phase to the disordered phase, colored according to the **ODO** scheme.

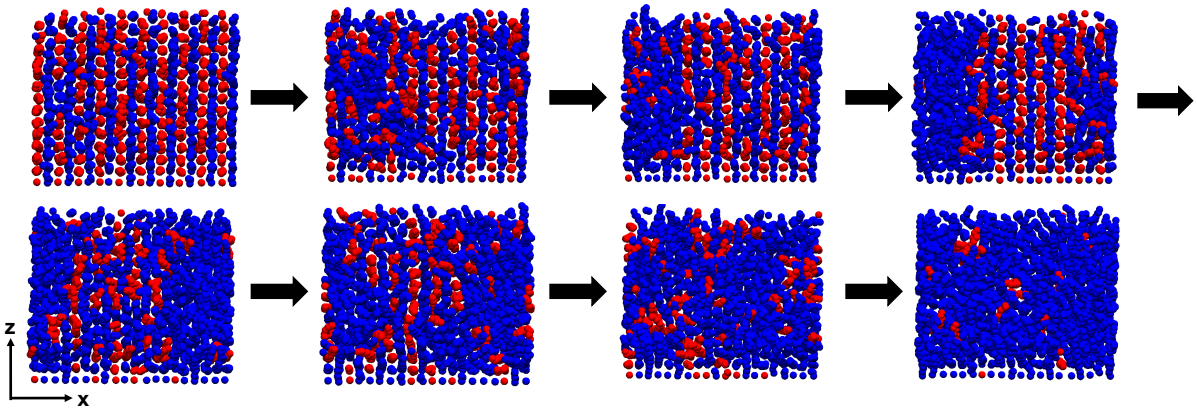

Figure 2.11: A progression of snapshots going from the ordered phase to the disordered phase, colored according to the **AG** scheme.

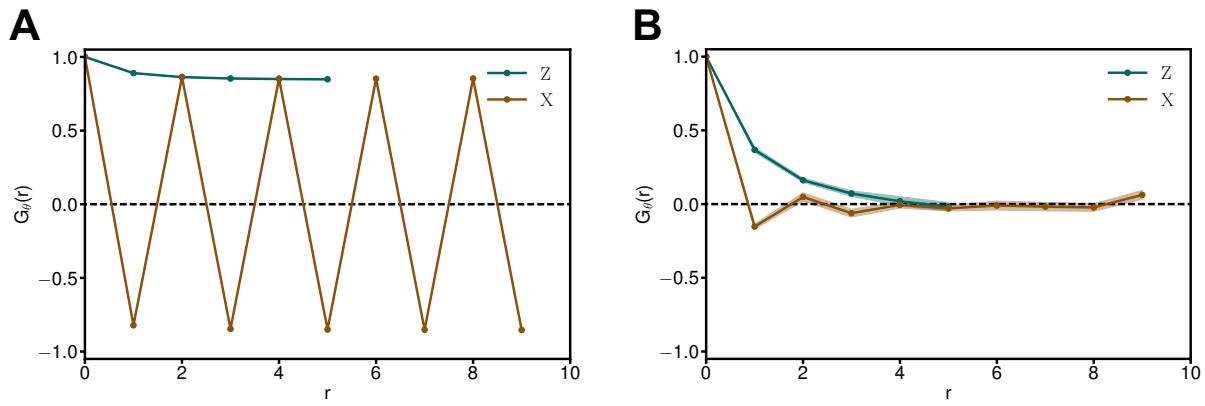

Figure 2.12: Spatial correlation functions $G_{\theta_{\text{vac}}}$ in the $x-$ and $z-$directions for the A) ordered and B) disordered phase at 365K and 400K, respectively. The ordered phase shows strong correlation and anti-correlation features due to the alternating pattern. Surprisingly, the disordered phase also has decaying oscillatory features in the $x-$direction.

400 K. This robustness suggests firstly that ordered patches are not slowly melting transients, but instead real features of the equilibrium state. Indeed, time correlation functions for ligand orientation,

$$G(\tau) = \Big\langle \big(x(\tau) - \bar{x}\big)\big(x(0) - \bar{x}\big) \Big\rangle_{\tau}, \tag{2.5}$$

decay rapidly at high temperature, as shown in Fig. 2.13 for the single ligand orientation $X = \theta_z$ and for the overall orientation $X = \Theta_z$. Robustness to heating secondly indicates that structural correlations in the disordered state are predominantly athermal, a consequence not of intermolecular cohesion but instead of constraints imposed by steric forces at high surface passivation.

MD simulation snapshots of the high-temperature ($T = 1000$ K) disordered phase were examined in detail to elucidate the structural aspects leading to oscillating correlations. The 100 ns simulation was divided into four equal time segments and each ligand's θ_z value was averaged across every 25 ns time slice. Each point in the new ligand lattice now represents an angle coarse-grained in time,

$$\theta_t(r_i) = \frac{1}{25 \text{ ns}} \sum_{t=0}^{25 \text{ ns}} \theta_z(r_i, t)$$

The four "average" configurations, shown in Fig. 2.14, were compared to each other and led to the following conclusions:

1. Each coarse-grained configuration has patches of structure, similar to the alternating pattern in the ordered phase. However, the magnitude of this oscillation is much smaller than in the ordered phase (note the scale of the color bar on the right in Fig. 2.14, indicating the typical range of the disordered Θ_z values). Rather than being a non-equilibrium result, these patches are a result of the system trying to adapt symmetry from the underlying rectangular CdS wurtzite lattice to form a hexagonal structure even in the disordered phase. The result is collective localized fluctuations in different regions where the ligands have θ_z values slightly above and below the thermal average, $\langle \theta_z \rangle_{\text{disord}}$, leading to decaying alternating spatial correlations in Fig. 2.12B.

2. These patches are not stationary; over time they migrate to different parts of the surface, ensuring translational symmetry of the equilibrium state. This mobility can be seen in Fig. 2.14, where each panel looks different than the others and structural features appear in different parts of the averaged configuration. Hence, the system eventually loses memory of its initial ligand orientations and explores phase space ergodically over the course of the simulation.

With this analysis, we concluded that the ligands were properly equilibrated, both in the ordered and disordered phases, while also discovering underlying structural aspects of the disordered phase.

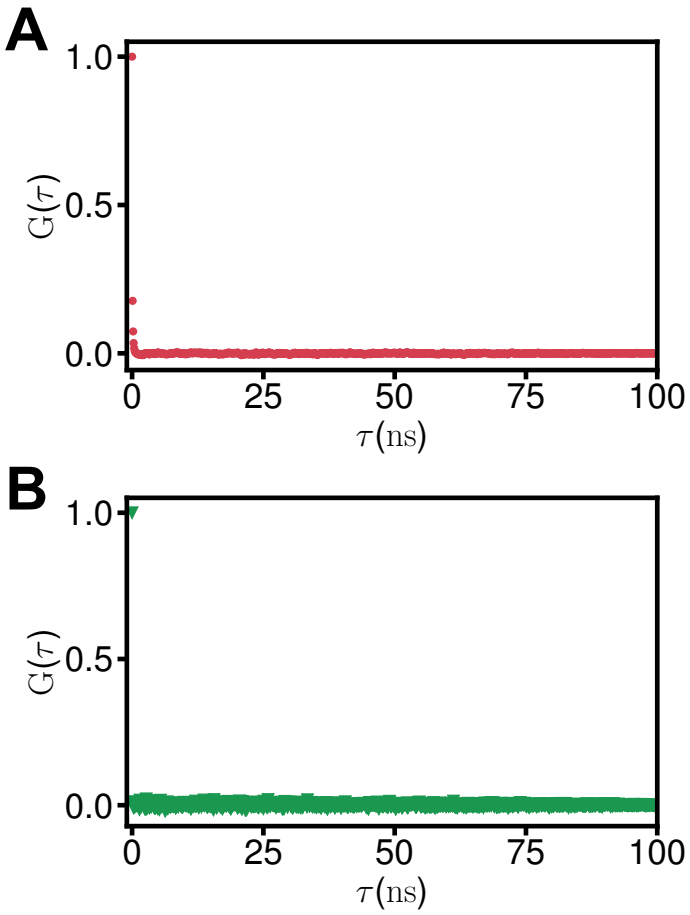

Figure 2.13: A) Time correlation function at 1000 K of the individual ligand orientation θ_z, showing rapid decay within a few nanoseconds, indicating that the system does not retain memory of the individual configuration over the course of the simulation. B) The same analysis for the order parameter, Θ_z, with a similar rapid time decay.

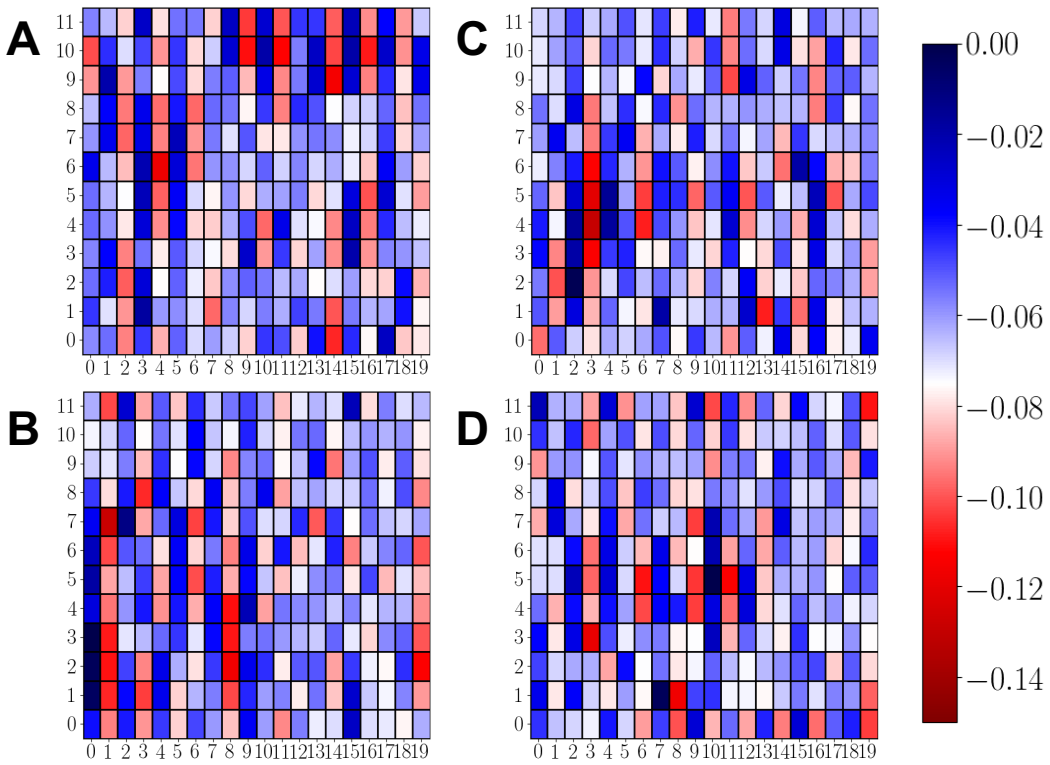

Figure 2.14: Each grid-point in each panel represents the time-averaged value of θ_z for every single ligand on the surface. The color bar used in displayed to the right, which assigns each ligand a color between -0.15 rad and 0.0 rad based on its time-averaged θ_z value. As can be observed, the lattice is not uniform, due to the structural features present in the disordered phase, and small patches of alternation are present in different regions of the surface each panel. A) This grid represents the time-averaged configuration over the first 25 ns of the MD simulation at 1000 K. B) A similar grid for the second 25 ns. C) The third 25 ns segment at 1000 K. D) The last 25 ns time-averaged block.

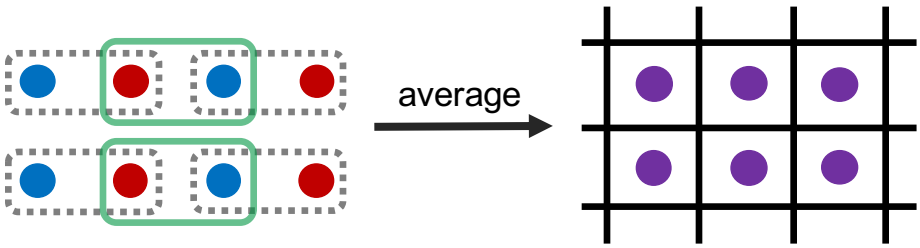

Figure 2.15: The transformation displayed above is used to convert the alternating features into a uniform configuration.

2.8 A simplifying transformation to remove correlation features

One goal of our MD simulations is to determine a correlation length for orientational fluctuations in ordered and disordered phases. Oscillation of the correlation functions $G_\theta(r)$, due to alternating *anti-gauche* patterns, complicates this task. In order to remove this feature, while preserving the essence of correlations near phase coexistence, we devised a new order parameter according to the scheme in Fig. 2.15. This transformation assigns a net orientation to each pair of ligands that are adjacent in the x direction,

$$\phi_z(r_{i+0.5}) = \frac{1}{2}\big(\theta_z(r_i) + \theta_z(r_{i+1})\big)\,. \tag{2.6}$$

The spatial average of this staggered parameter is identical to the original order parameter, $\Theta_z = \Phi_z$. But for a perfectly alternating configuration, $\{\phi_z(r_i)\}$ is spatially uniform. Fig. 2.16 shows the staggered field, coarse-grained over a time of 10 ns, for ordered and disordered states.

The ordered and disordered θ_z-configurations from the MD simulations were compared with their ϕ_z-equivalents, shown in Fig. 2.16. The **ODO** coloring scheme was used to distinguish between the two phases and resulted in more uniform lattices without the finer structural aspects, while still displaying the phase transition.

For the ordered phase, the spatial correlation function of the staggered field G_ϕ decays monotonically as desired, as shown in Fig. 2.17A. In this case our transformation enables simple extraction of a correlation length. For the disordered phase, however, fluctuations in ϕ_z retain an oscillatory character in the x direction. As can be seen in Fig. 2.16, ordered patches within the disordered phase do not exhibit the same coherence as the low-temperature phase. Paired defects in *anti-gauche* alternation, which register as anticorrelation in the staggered field, are common in these patches. Both Θ_z and Φ_z were used to further explore ligand properties, as will be explained in the subsequent chapters.

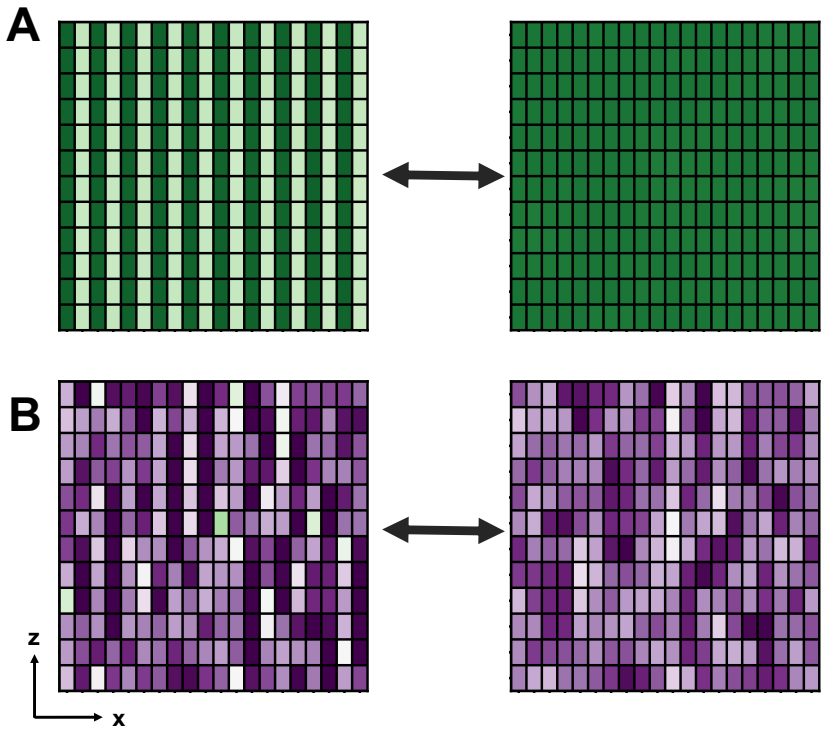

Figure 2.16: The transformation of the lattice using Eq. 2.6. A) The ordered phase, coarse-grained in time and represented as a grid, becomes uniform under this transformation. B) The time-coarse-grained disordered phase from MD simulations and the corresponding result after using Eq. 2.6. All configurations are colored according to the **ODO** scheme, and the ordered phase, though more uniform than when viewed in the **AG** scheme, still shows alternating stripes due to the C-C bond conformations.

2.9 Solvent simulation details and resulting configurations

The results we have presented so far were obtained from simulations of surface-bound ligands in vacuum, i.e., in the absence of solvent. We performed analogous calculations with an explicit collection of solvent molecules in order to understand how the ligands' ordering behavior is sensitive to the structure of their surroundings. The chosen solvent was hexane, as the C_{18} molecules and hexane are both non-polar and have similar dispersion interactions. The similarity in their inter-molecular forces creates an interesting interplay between ligand ordering and maximizing ligand-solvent contacts.

Like the ligands, hexane is a straight chain alkane. The same LAMMPS setup and parameters as in Section 2.2-2.3 were used to represent solvent interactions with itself as well

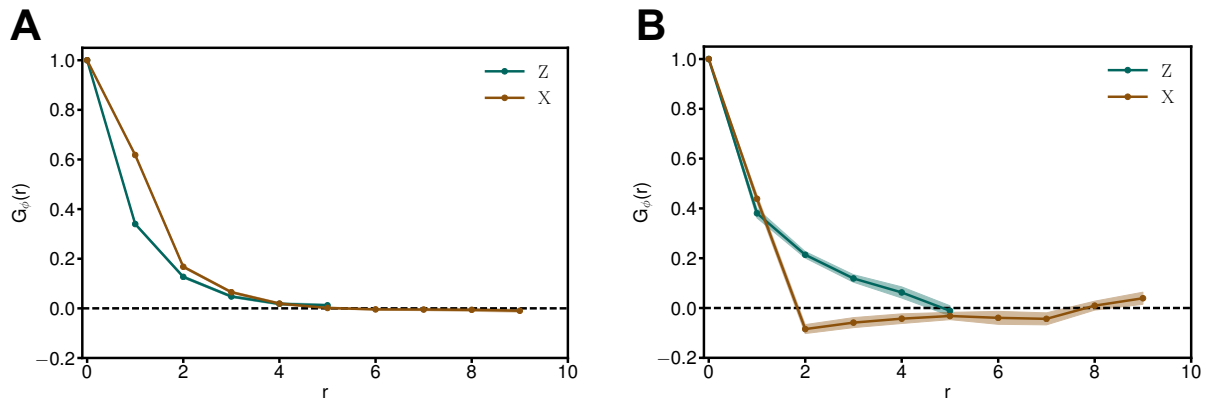

Figure 2.17: Spatial correlation functions $G_{\phi_{\text{vac}}}$ for the averaged orientation angle ϕ_z in the $x-$ and $z-$ directions for the A) ordered and B) disordered phase at 365K and 400K, respectively. The strong oscillatory patterns are not present anymore; however, some remnants of the structure are seen in the $x-$ direction correlation trends.

as with C_{18} chains and perform MD simulations. In solvent, ligands in the ordered phase still tend to align in alternating rows, and we observe defect states similar to those in vacuum Hence, biased replica exchange was used to achieve equilibrium sampling of both the phases and to determine their relative weights at different temperatures. Equilibrium configurations obtained for both phases are shown in Fig. 2.18. The corresponding probability distributions for θ_z and Θ_z in each phase are shown in Fig. 2.19.

The spatial correlation functions in θ_z were computed for both phases. These are plotted in Fig. 2.20. The presence of solvent decreases the amplitude of the oscillating correlation trend in the disordered phase $G_{\theta_{\text{disord,solv}}}$ as compared to the vacuum $G_{\theta_{\text{disord,vac}}}$. The corresponding ligand configuration grids and spatial correlation functions for the order parameter Φ_z are plotted in Figs. 2.21 and 2.22, respectively.

The ordered phase correlations are similar in solvent and vacuum, with $G_{\theta_{\text{ord,solv}}}$ and $G_{\theta_{\text{ord,vac}}}$ decaying over a comparable length scale of 2 ligand units away, as seen in Figs. 2.12 A and 2.20 A. The tightly packed ordered structure offers no space for solvent molecules to intrude, again highlighting the essential role of steric interactions in ligand ordering.

The disordered phase, however, shows differing structure in vacuum and solvent. Specifically, the correlation function $G_{\theta_{\text{disord,solv}}}$ does not show a strong oscillatory trend in the $x-$direction, more closely resembling the vacuum result $G_{\phi_{\text{disord,solv}}}$ for the transformed order parameter (see Figs. 2.12 B and 2.20 B). The implied disruption of *anti-gauche* alternation is accompanied by intercalation of solvent molecules into the disordered ligand layer, as described below.

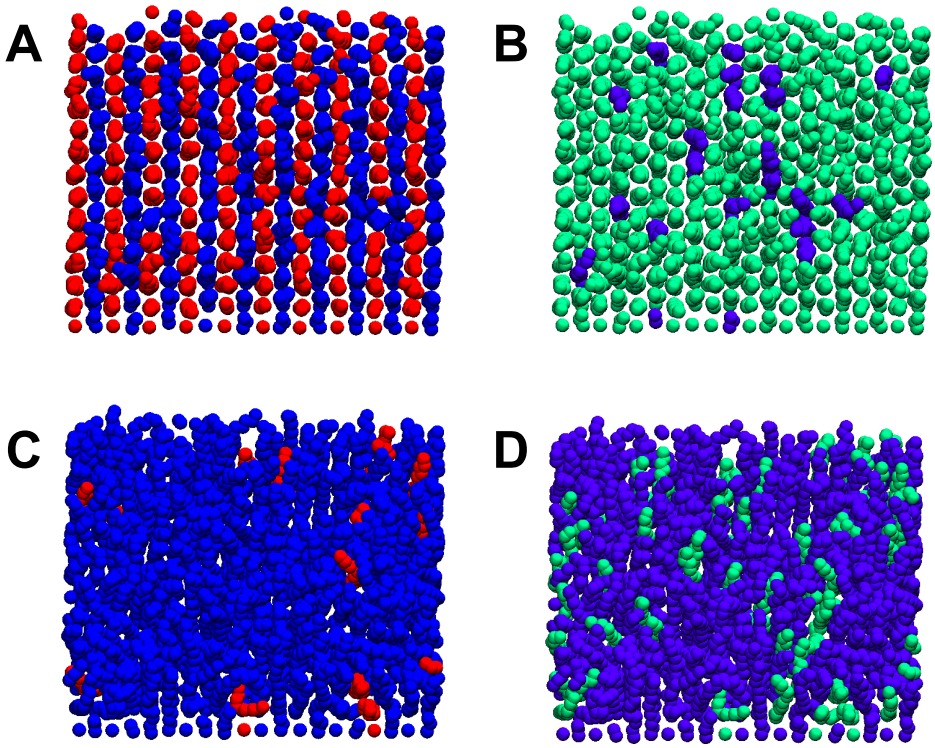

Figure 2.18: Equilibrium ligand configurations for simulations in hexane in the ordered phase, colored according to the A) **AG** and B) **ODO** schemes. C, D) The same coloring schemes applied to the disordered phase.

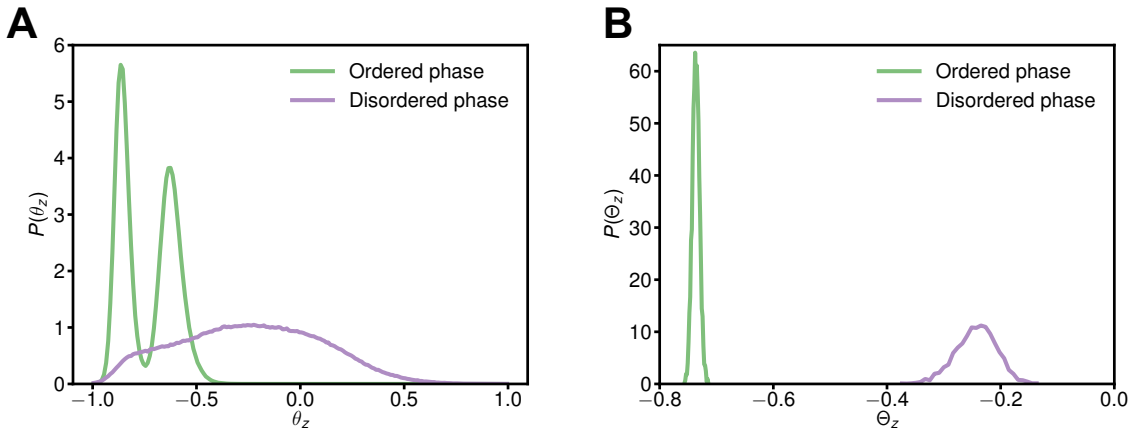

Figure 2.19: A) Probability distribution of θ_z in the ordered and disordered phases in solvent. B) The same distributions, but this time for Θ_z.

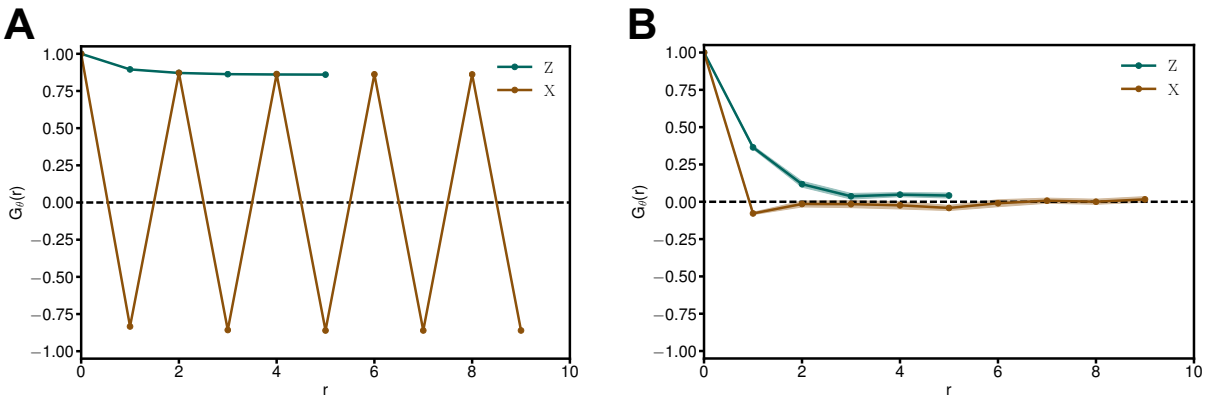

Figure 2.20: Spatial correlation functions $G_{\theta_{\text{solv}}}$ of the ligand orientation in the $x-$ and $z-$directions for the A) ordered and B) disordered phase at 360K and 375K, respectively. The anti-correlation trend in the $x-$direction is strong in the ordered phase, but not so in the disordered phase - this is an effect of the hexane molecules.

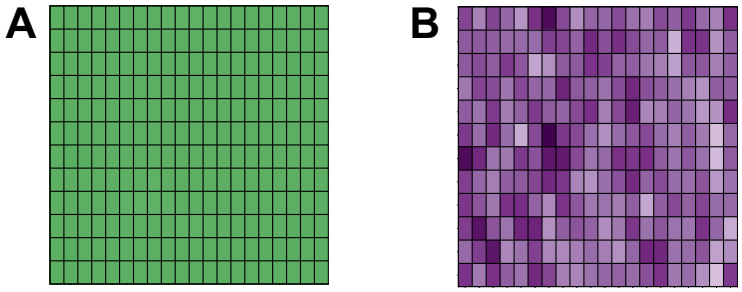

Figure 2.21: Lattices representing the ϕ_z values in the A) ordered and B) disordered phases in hexane.

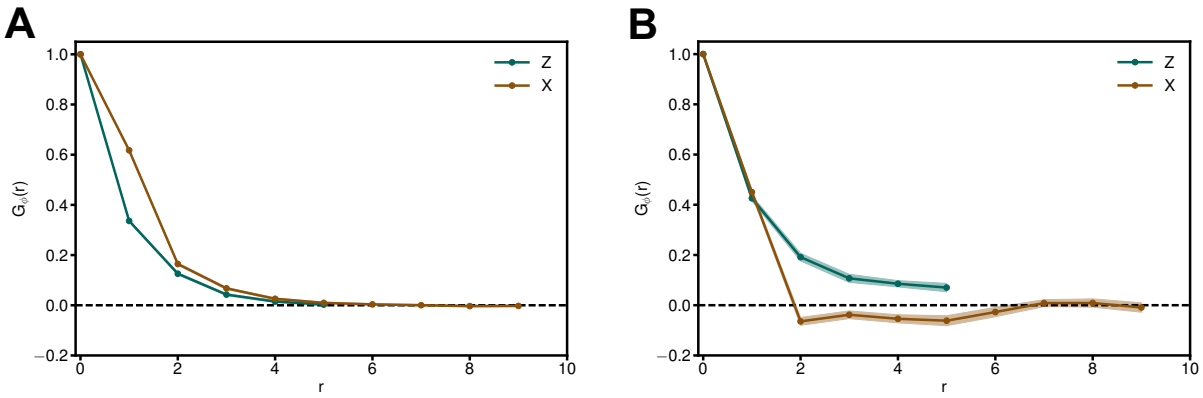

Figure 2.22: Spatial correlation functions $G_{\phi_{\text{solv}}}$ for the block-averaged angle ϕ_z in the $x-$ and $z-$directions for the A) ordered and B) disordered phase at 360K and 375K, respectively. The oscillation trends in the $x-$direction in the ordered phase have been removed, like in vacuum, but the disordered phase $G_x(r)$ look very similar for both θ_z and ϕ_z.

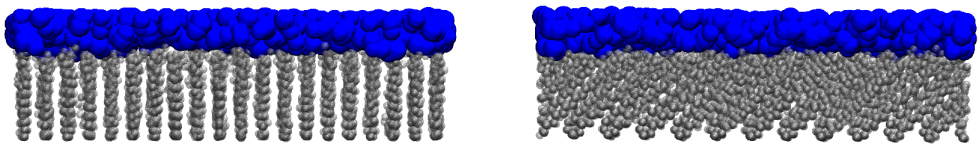

Figure 2.23: Snapshots depicting solvent (in blue) near the ligand layer (in grey) in the ordered phase. Two different viewing angles show that hexane molecules do not penetrate the ligand layer, instead collecting at the tips of the octadecyl chains.

Changes in disordering mechanism due to solvent inclusion in ligand layer

Figs. 2.23 and 2.24 show representative snapshots from MD simulations of ligand layers in hexane. In the ordered phase, ligands are very densely packed and exclude solvent completely. Similarity with the vacuum case is underscored by nearly identical values for the order parameter,

$$\langle\theta_z\rangle_{\text{ord,solv}} = \langle\theta_z\rangle_{\text{ord, vac}} = -0.74 \text{ rad}\,,$$

In the disordered phase, however, the orientational order parameter is less negative in solvent than in vacuum:

$$\langle\theta_z\rangle_{\text{disord,solv}} = -0.25 \text{ rad}$$

as compared to

$$\langle\theta_z\rangle_{\text{disord, vac}} = -0.30 \text{ rad}\,.$$

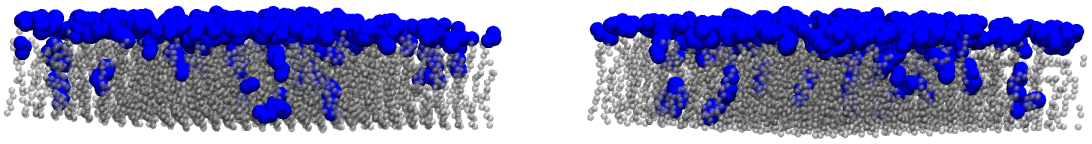

Figure 2.24: Snapshots showing hexane (in blue) in and around the ligands (in grey) in the disordered phase. As can be observed, there is a lot more solvent penetrating into the ligand layer, which is stabilized by the favorable dispersion forces between hexane and the C_{18} chains. The interspersed solvent molecules disrupt localized ordering patterns in the disordered phase.

Geometrically, this comparison indicates that the ligands extend more vertically in the presence of hexane. The ligand layer becomes less densely packed as a result. Weighing against this change is a decline in the number of ligand-ligand contacts. In hexane, the corresponding loss of cohesive energy within the ligand layer can be compensated by favorable dispersion interactions between hexane and octadecyl molecules. These energetic biases largely offset, so that expansion of the disordered ligand layer in solvent is neither very costly nor very beneficial. Entropically, penetration of solvent into the ligand layer restricts the conformational freedom of octadecyl molecules. On the other hand, the intruding solvent molecules gain translational freedom. These entropic biases also largely offset. The thermodynamic stabilities of ordered and disordered phases are therefore little changed by the introduction of solvent, despite appreciable structural modifications in the disordered state.

In the above-described ways, MD simulations provide insight into ligand behavior on nanoparticle surfaces in vacuum and solvent. Another approach is to use a simple first-principles approach to model the first-order phase transition, which is detailed in the next chapter.

Chapter 3

Field theoretic model of a first-order phase transition

Ligand ordering can also be modeled using the general characteristics associated with a phase transition. In order to do so, we propose a field theory with a Hamiltonian describing the interactions of the $\Theta_z(\mathbf{r})$ order parameter field on a CdS surface. The advantage of postulating a Hamiltonian that governs field interactions is that it lends considerable simplicity to the system studied by removing microscopic details. This also significantly reduces computational costs associated with performing MD simulations of several thousands of particles. Different realizations of the field represent different states of the system and averaging over these realizations leads to thermodynamic properties of the system. Phase transitions occur at the points in phase space where one of these calculated properties is non-analytic; these transitions can be first- or second-order. A first-order phase boundary has the attributes given here:

1. The change in the order parameter at the phase transition is discontinuous.
2. The correlation length, however, is finite, since it is not a critical point.
3. Two or more phases may coexist in equilibrium at the transition point.

On the other hand, a second-order phase transition has the following features:

1. A continuous change of the order parameter value at the phase boundary
2. A diverging susceptibility and infinite correlation length at the critical point

The ligands examined in this work undergo a transition that is first-order; as temperature changes, the mean orientation angle changes discontinuously from the ordered to the disordered value. The following postulated model is defined by a minimally detailed free energy functional that represents the characteristics of such a phase transition parameterized by simulation data.

3.1 Postulated free energy for ligand ordering inspired by Landau-Ginzburg theory

Landau-Ginzburg theory [14, 24], a broadly used classical phenomenological field theory for symmetry breaking, was postulated as a simple description of superconductivity. Since it is phenomenological in nature, it is not always accurate in predicting critical quantities and specific details of the system. However, its simple Hamiltonian holds appeal for examining the general features associated with a phase transition of interest, e.g., orientational ordering of ligands.

Microscopic fluctuations in this description are represented by a field $\eta(\mathbf{r})$ describing the extent of local order at each position in space. A given realization this field has a statistical weight $z[\eta(\mathbf{r})] \propto \mathrm{e}^{-\beta\mathcal{H}[\eta(\mathbf{r})]}$, where $\mathcal{H}$ an effective Hamiltonian for spatially varying fluctuations of the order parameter. Strictly, its form follows from the detailed microscopic Hamiltonian after integrating out all fluctuations subject to a constraint on $\eta(\mathbf{r})$. The spirit of the Landau-Ginzburg approach is to motivate the essential form of the functional $\mathcal{H}[\eta(\mathbf{r})]$ at a coarse level, with special attention to pertinent symmetries. The total partition function $\mathcal{Z}(T)$ is computed in principle as a functional integral of $z[\eta(\mathbf{r})]$ over all possible realizations of $\eta(\mathbf{r})$,

$$\mathcal{Z}(T) = \int \mathcal{D}[\eta(\mathbf{r})] \exp\left(-\beta \int d\mathbf{r}\, \mathcal{H}[\eta(\mathbf{r})]\right). \tag{3.1}$$

The corresponding free energy for this equilibrium state is then obtained as a logarithm of $\mathcal{Z}$,

$$\mathcal{F} = \frac{-\ln \mathcal{Z}}{\beta} \tag{3.2}$$

Following the standard development, we describe separately contributions to $\mathcal{H}[\eta(\mathbf{r})]$ that are spatially local and those that depend on variations of $\eta(\mathbf{r})$ with $\mathbf{r}$. The local contribution involves a function of the order parameter $f(\eta)$, which notionally represents the free energy density of a spatially uniform state in which the order parameter adopts the value η everywhere. We evaluate this local potential at each point in space according to the local value of the order parameter, then sum over all points in space to obtain $\int d\mathbf{r}\, f(\eta(\mathbf{r}))$. The non-local contribution primarily serves to penalize rapid spatial variation of the field. The simplest form involves the squared gradient of $\eta(\mathbf{r})$, integrated over space to give $\int d\mathbf{r}\, \kappa|\nabla\eta(\mathbf{r})|^2/2$. The coefficient κ sets the thermodynamic cost of gradients in $\eta(\mathbf{r})$; it strongly influences correlation lengths and interfacial tension that emerge from the field theory.

Our full effective Hamiltonian governing fluctuations in $\eta(\mathbf{r})$ is thus,

$$\mathcal{H}[\eta(\mathbf{r})] = \int d\mathbf{r} \left(f(\eta'(\mathbf{r})) + \frac{\kappa}{2}|\nabla\eta'(\mathbf{r})|^2\right). \tag{3.3}$$

Further progress requires a specific form of the local free energy density $f(\eta)$.

Polynomial expansion of field theoretic Hamiltonian and resulting free energy

To capture the first-order ligand phase transition, the homogeneous free energy density $f(\eta)$ should follow the basic progression of energy landscapes shown in Fig. 3.1. Most importantly, the location of the global minimum changes discontinuously as temperature increases through a transition value T_t. The progression of Fig. 3.1 can be achieved most simply by taking $f(\eta)$ to be a polynomial in η, whose coefficients $A_i(T)$ change appropriately with temperature,

$$f(\eta) = \sum_{i=0}^{i_{\max}} A_i(T)\, \eta^i \,.$$

The double-well structure of $f(\eta)$ requires that this polynomial be at least fourth-order in complexity, i.e., $i_{\max} \geq 4$. For simplicity, we truncate the expansion precisely at fourth order, taking $i_{\max} = 4$. The coefficient of the highest-order term must be always positive to ensure stability, and the existence of two stable wells separated by a barrier requires that the coefficient of the quadratic term be negative. Because these coefficients do not approach zero or change sign, we take them to be constant: $A_2(T) = a < 0$ and $A_4(T) = c > 0$, both independent of temperature.

Precisely at $T = T_t$, our model free energy density is symmetric about $\eta = 0$, so that all odd-order coefficients must vanish, $A_1(T_t) = A_3(T_t) = 0$. A discontinuous change in the free-energy-minimizing order parameter value requires that one of the odd-order coefficients change sign at T_t. We choose the linear-order term for this purpose,

$$A_1(T) = (T - T_t)h \,,$$

where h is a negative constant, and set $A_3(T) = 0$ at all T. A qualitatively similar progression in $f(\eta)$ could be obtained by instead including the cubic contribution in place of the linear term; however, we find that agreement of such a progression with results of ligand simulations is generally poorer.

Our local free energy density therefore takes the simple form

$$f(\eta) = h\,(T - T_t)\,\eta + \frac{a}{2}\,\eta^2 + \frac{c}{4}\,\eta^4 \,,$$

and the full effective Hamiltonian becomes,

$$\boxed{\mathcal{H}\left[\eta(\mathbf{r})\right] = \int d\mathbf{r}\left[h\,(T - T_t)\,\eta(\mathbf{r}) + \frac{a}{2}\,\eta(\mathbf{r})^2 + \frac{c}{4}\,\eta(\mathbf{r})^4 + \frac{\kappa}{2}\,|\nabla\eta(\mathbf{r})|^2\right]}. \tag{3.4}$$

This field theory is completely parameterized by the phenomenological constants h, a, c, and κ.

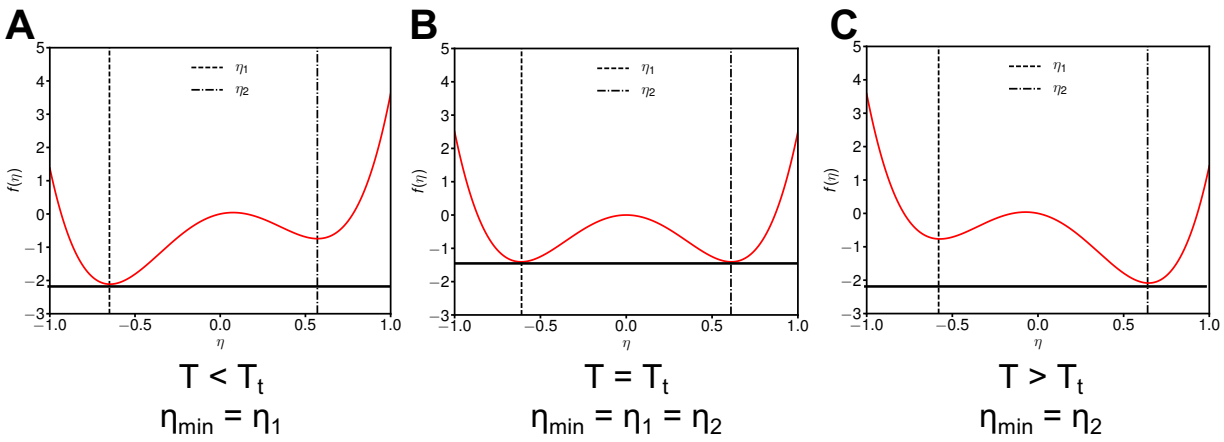

Figure 3.1: A schematic of a first-order transition, shown in the potential energy-order parameter space. As temperature varies, the lowest energy order parameter value undergoes a discontinuous shift, tracking the features of a first-order phase transition.

Saddle point approximation

Despite its simple ingredients, the field theory described by Eq. 3.4 is complex and rich, supporting critical fluctuations and non-analytic transitions in the thermodynamic limit. Correspondingly, it is very difficult to analyze formally. Computer simulations of a discretized form are straightforward, but our purposes are better suited by an approximate analysis that captures the essence of phase transitions in this model.

Great simplification can be achieved by making a saddle point approximation for the functional integral in Eq. 3.1. This estimate focuses on a single realization of the order parameter field, the one that has the largest statistical weight. Using this approximation, we obtain,

$$\begin{aligned} \mathcal{F} &\approx \int d\mathbf{r}\, \mathcal{H}[\bar{\eta}(\mathbf{r})]\,. \\ \implies \mathcal{F} &= \int d\mathbf{r} \left(h\,(T - T_t)\,\bar{\eta}(\mathbf{r}) + \frac{a}{2}\,\bar{\eta}(\mathbf{r})^2 + \frac{c}{4}\,\bar{\eta}(\mathbf{r})^4 + \frac{\kappa}{2}\,|\nabla\bar{\eta}|^2 \right]. \end{aligned} \tag{3.5}$$

Here, $\bar{\eta}(\mathbf{r})$ denotes the function that maximizes $z[\eta(\mathbf{r})]$ or, equivalently, minimizes the functional $\mathcal{H}[\eta(\mathbf{r})]$. All fluctuations about this ground state are neglected. This procedure amounts to a mean field approximation, and reduces the mathematical problem to a functional minimization of the effective Hamiltonian $\mathcal{H}\,[\eta(\mathbf{r})]$. The analysis below relies on this saddle point approximation throughout. For notational simplicity, however, we will use $\eta(\mathbf{r})$ in place of $\bar{\eta}(\mathbf{r})$. It is implied that the fields of interest are those that minimize $\mathcal{H}\,[\eta(\mathbf{r})]$.

In the absence of boundary conditions or a spatially varying external field, the saddle

point approximation is particularly simple. In this case, the ground state must be spatially uniform, so that $\eta(\mathbf{r}) = \text{const}$ and $\nabla\eta(\mathbf{r}) = 0$. The mean field solution is then obtained simply by minimizing the function $f(\eta)$. For our polynomial form of $f(\eta)$, this minimization can be performed exactly.

When boundary conditions impose spatial variation on the mean field $\eta(\mathbf{r})$, the saddle point approximation instead requires solving a problem of functional variation. We will do so in the standard way by recasting the variational problem as an Euler-Lagrange equation.

3.2 Parameterization of field theory using a mean-field approach

The field theory postulated in Eq. 3.5 describes a generic system with order parameter field $\eta(\mathbf{r})$. To make connection with the C_{18} ligand systems of interest, we need to assign appropriate values to the parameters h, T_t, a, c and κ. Because these quantities are phenomenological, they cannot be directly measured, either in experiment or simulation. But their values determine statistical properties of the field theory that do correspond to observable features of the detailed physical system. We proceed by deriving these relationships from the field theory, computing the same quantities from MD simulation, and inferring parameter values that ensure agreement between the two.

There are five unknown scalar parameters in the field theoretic Hamiltonian; therefore, one needs to calculate five properties to be able to fully constrain the model. The properties we computed for our model are:

1. Transition temperature, T_t
2. Difference $\Delta\eta(T_t)$ between the order parameter values of each phase at T_t
3. Entropy difference ΔS between the two equilibrium phases at T_t
4. Surface tension σ between the phases of interest at T_t
5. Correlation decay length λ at temperature T_t

The calculation of each of these properties is outlined below.

Transition temperature

At temperature T_t, our polynomial model of the homogeneous free energy density $f(\eta)$ is completely symmetric about $\eta = 1/2$. In particular, $f(\eta)$ has two degenerate minima, suggesting a state of phase coexistence. Indeed, mean field theory predicts a first order transition at precisely this temperature.

In the full field theory, symmetry breaking is not guaranteed at T_t. Fluctuations neglected by the saddle point approximation could disrupt a state of coexistence, rendering the homogeneous state stable despite the double-well form of $f(\eta)$. Since we are focusing on a mean-field approach to the field theory, we will regard T_t as the exact transition temperature for ligand ordering.

Order parameter difference

The two coexisting phases at the transition temperature T_t are characterized by distinct values of the order parameter, η_1 and η_2. These two values locate the minima of $f(\eta)$. They can be determined by differentiation.

At the extrema of $f(\eta)$,

$$\begin{aligned} \left.\frac{df}{d\eta}\right|_{T_t} &= a\eta + c\eta^3 = 0 \\ \implies \eta &= 0,\ \pm\sqrt{\frac{|a|}{c}}\,. \end{aligned} \tag{3.6}$$

The first root, $\eta = 0$, corresponds to a maximum in $f(\eta)$. The other two roots are guaranteed to be real, since $c > 0$. The coexisting phases therefore have order parameter values,

$$\begin{aligned} \eta_1 &= -\sqrt{|a|/c} \\ \eta_2 &= +\sqrt{|a|/c}\,. \end{aligned} \tag{3.7}$$

The difference between these two values,

$$\boxed{\Delta\eta \equiv \eta_2 - \eta_1 = 2\sqrt{\frac{|a|}{c}}}\,, \tag{3.8}$$

is set by the field theory parameters a and c.

Entropy difference

The entropy is obtained by taking a derivative of the free energy with respect to temperature in each phase.

$$S = -\left.\frac{d\mathcal{F}}{dT}\right|_{\min\,\mathcal{F}} = -A\left(h\eta + \frac{d\mathcal{F}}{d\eta}\frac{d\eta}{dT}\right) = -Ah\eta\,,$$

where A is the area of the substrate on which the ligands are bound.

When $\mathcal{F}$ is minimized, $d\mathcal{F}/d\eta = 0$ and thus, the only non-zero term comes from the temperature-dependent linear field. Evaluating S at the order parameter values calculated above yields,

$$\boxed{\Delta S \equiv S(\eta_2) - S(\eta_2) = -2Ah\sqrt{\frac{c}{|a|}}}\,. \tag{3.9}$$

Surface tension

Surface tension σ is the free energy cost, per unit surface, of developing an interface between two phases at conditions of coexistence. We determine σ from our field theory by comparing the free energies of systems with and without an interface, at the transition temperature T_t.

The free energy $\mathcal{F}_{\rm homo}$ of a single homogeneous phase (lacking any interface) is simply $\mathcal{F}_{\rm homo} = Af(\eta_1) = Af(\eta_2)$.

Introducing an interface in mean field theory requires boundary conditions that establish distinct bulk phases on two sides of the system. Taking x to be the direction perpendicular to the interface, we impose,

$$\begin{aligned} \eta(x = -\infty, z) &= \eta_1 \\ \eta(x = +\infty, z) &= \eta_2 \,. \end{aligned} \tag{3.10}$$

For each value of x, the system remains homogeneous in the direction z parallel to the interface, i.e., $\eta(\mathbf{r}) = \eta(x)$. The effective Hamiltonian can therefore be written as,

$$\mathcal{H}[\eta(x)] = L_z \int dx \Big(\frac{a}{2}\,\eta(x)^2 + \frac{c}{4}\,\eta(x)^4 + \frac{\kappa}{2} \Big| \frac{d\eta(x)}{dx} \Big|^2 \Big) \,, \tag{3.11}$$

where L_z represents the length of the system in the $z-$direction. The mean-field solution minimizes this functional. Equivalently, it solves the Euler-Lagrange equation,

$$\begin{aligned} \frac{\partial \mathcal{H}}{\partial \eta(x)} &= a\eta(x) + c\eta(x)^3 - \kappa \frac{d^2\eta(x)}{dx^2} = 0 \\ &\implies a\eta(x) + c\eta(x)^3 = \kappa \frac{d^2\eta(x)}{dx^2} \,. \end{aligned} \tag{3.12}$$

subject to the boundary conditions above. This boundary value problem has a known solution, $\boxed{\eta(x) = \eta_0 \tanh\left(x/l_0\right)}$ where $l_0 = \sqrt{2\kappa/|a|}$. The variation of $\eta(x)$ in the $x-$direction is shown schematically in Fig. 3.2. The saddle-point order parameter profile $\eta(x)$ gives a free energy $\mathcal{F}_{\rm int} = \mathcal{H}[\eta(x)]$ for coexisting phases separated by an interface. Integrating by parts and applying the boundary conditions, the gradient term becomes

$$\int dx \frac{\kappa}{2} |\nabla \eta|^2 = -\int dx \frac{\kappa}{2} \eta \, \frac{d^2\eta}{dx^2} \,.$$

Subtracting the homogeneous free energy from the interfacial free energy, we obtain a surface tension as,

$$\sigma = \frac{\mathcal{F}_{\rm int} - \mathcal{F}_{\rm homo}}{L_z} = \int dx \, f(\eta(x)) + \frac{\kappa}{2} |\nabla \eta(x)|^2 - f(\eta_{1,2}) \,, \tag{3.13}$$

where $f(\eta) \equiv h(T - T_t)\eta + a\eta^2/2 + c\eta^4/4$ and at T_t, $f(\eta) = a\eta^2/2 + c\eta^4/4$. $f(\eta_{1,2})$ refers to the value of $f(\eta)$ in the free energy minima of the homogeneous phases. At the transition

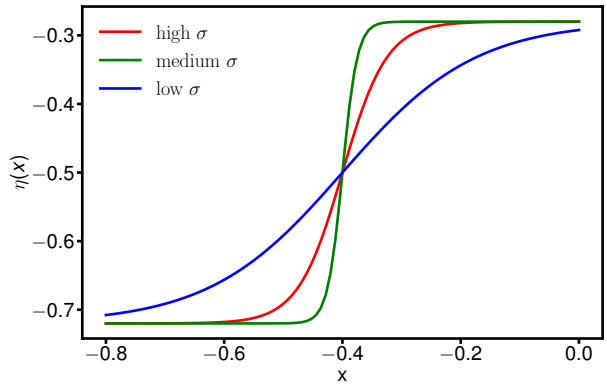

Figure 3.2: A schematic showing the order parameter profile that minimizes the system's free energy under the boundary conditions in Eq. 3.11.

temperature, $f(\eta_{1,2})$ is the same for both phases as they are in coexistence. Using integration by parts and the fact that η is constant at the boundaries, one can derive that

$$\int dx \frac{\kappa}{2} |\nabla \eta|^2 = - \int dx \frac{\kappa}{2} \eta \, \frac{d^2 \eta}{dx^2} \, .$$

Using Eq. 3.13 and Eq. 3.7, we find that the surface tension is given by,

$$\boxed{\sigma = \frac{2\sqrt{2}}{3c} \sqrt{\kappa \, |a|^3}} \, . \tag{3.14}$$

Correlation length

Lastly, the correlation length is the characteristic decay length associated with the spatial correlation function $G(|\mathbf{r} - \mathbf{r}'|) = \langle \delta\eta(\mathbf{r}) \delta\eta(\mathbf{r}') \rangle$. Here $\delta\eta(\mathbf{r}) \equiv \eta(\mathbf{r}) - \eta_{1,2}$, where $\eta_{1,2}$ denotes the order parameter value in the appropriate bulk equilibrium phase.

Due to translational symmetry, the two-point correlation function $G(\mathbf{r} - \mathbf{r}')$ is diagonal in reciprocal space, i.e., its Fourier transform depends on a single wavevector $\mathbf{q}$. Defining Fourier components of the order parameter field as $\delta\eta(\mathbf{r}) = \sum_q \delta\hat{\eta}_q e^{i\mathbf{q}\cdot\mathbf{r}}$ and $\delta\hat{\eta}_q^* = \delta\hat{\eta}_{-q}$, we can write,

$$\begin{aligned} G(q) &= \int d\mathbf{r} \int d\mathbf{r}' G(|\mathbf{r} - \mathbf{r}'|) \, e^{i\mathbf{q}\cdot(\mathbf{r}-\mathbf{r}')} \\ &= \left\langle \int d\mathbf{r} \int d\mathbf{r}' \sum_{q'} \sum_{q''} \delta\hat{\eta}_{q'} \, \delta\hat{\eta}_{q''} \, e^{i(\mathbf{q}+\mathbf{q}')\cdot\mathbf{r}} e^{i(\mathbf{q}''-\mathbf{q})\cdot\mathbf{r}'} \right\rangle \\ &= A^2 \langle \delta\hat{\eta}_q \, \delta\hat{\eta}_{-q} \rangle = A^2 \langle |\delta\hat{\eta}_q|^2 \rangle \, . \end{aligned} \tag{3.15}$$

From our field theory, $G(\mathbf{r}-\mathbf{r}')$ can be determined by calculating the response to a spatially varying external field and appealing to the fluctuation dissipation theorem. The saddle point approximation again requires solving a problem of functional variational, or its equivalent Euler-Lagrange equation. Alternatively, an equivalent result can be obtained more simply by expanding the effective Hamiltonian $\mathcal{H}[\eta(\mathbf{r})]$ about the uniform mean field solution.

To quadratic order in $\delta\eta$, the field theory Hamiltonian can be written

$$\mathcal{H}[\delta\hat{\eta}_q] = Af(\eta_{1,2}) + A\sum_q |\delta\hat{\eta}_q|^2\Big(\frac{a}{2} + \frac{3c}{2}\,\eta_{1,2}^2 + \frac{\kappa}{2}q^2\Big) + \mathcal{O}(\delta\eta^3)\,,$$

Within this harmonic approximation, the probability distribution for order parameter fluctuations is $z[\delta\hat{\eta}_q] \propto e^{-\beta\Delta\mathcal{H}} \propto e^{-\beta\sum_q |\delta\hat{\eta}_q|^2(P+\kappa q^2/2)}$, where $P \equiv \dfrac{a}{2}+\dfrac{3c}{2}\,\bar{\eta}^2$. Using the equipartition theorem, we then obtain,

$$\begin{aligned} \frac{k_BT}{2} &= V\langle|\delta\hat{\eta}_q|^2\rangle\Big(P+\frac{\kappa}{2}q^2\Big) \\ \implies \langle|\delta\hat{\eta}_q|^2\rangle &= \frac{k_BT}{2V\Big(P+\frac{\kappa}{2}q^2\Big)}\,. \end{aligned} \tag{3.16}$$

Transforming the correlation function back to real space (in two spatial dimensions), we find that,

$$G(r) = \frac{k_BT\pi}{P\lambda^2}K_0\Big(\frac{r}{\lambda}\Big)\,, \tag{3.17}$$

where $K_0(r)$ is the zeroth order modified Bessel of the second kind. This is an exponentially decaying function with a decay length λ, which is related to the field theoretic parameters as,

$$\boxed{\lambda = \sqrt{\frac{\kappa}{|a|}}}\,. \tag{3.18}$$

Thus, we have relations for all the physical quantities that we need to parameterize the field theory. Using Eqs. 3.8, 3.9, 3.14 and 3.18, and calculating the corresponding properties from MD simulations gives us a set of equations to obtain h, T_t, a, c and κ for the ligand ordering phase transition. Each of the field theoretic results has been obtained within a saddle point approximation, and may therefore not be quantitatively faithful to the full field theory. Because our ligand system is far from a critical point, however, the qualitative foundations of mean field theory should be sound. Provided these relationships are used within the context of mean-field analysis, the resulting field theory should be a reasonable and internally consistent caricature of the physical system.

3.3 Other potential ways to parameterize field theory Hamiltonian

We have formulated a different way to parameterize the field theory, based on numerical simulations of the fluctuating nonlinear model. Because it does not rely on approximation, the result should be more faithful to the full field theory. Because it is much more cumbersome, however, and because it lacks the generality of the analytical relationships presented above, we have not pursued it in practice. Here we provide only an outline of the approach.

This method is based on the likelihood $\mathcal{L}$ of observing a proposed set of model parameters given the data observed in simulations. This likelihood can be maximized to find the optimal set of parameters for a given set of simulation data. The field theoretic Hamiltonian, along with probability of observing a given field $\eta(\mathbf{r})$, is,

$$\begin{aligned} \mathcal{F}_M[\eta(\mathbf{r})] &= \int d\mathbf{r}\Big[f_M[\eta(\mathbf{r})] + \frac{\kappa}{2}|\nabla\eta(\mathbf{r})|^2\Big] \\ \implies P_M[\eta(\mathbf{r})] &= \frac{e^{-\beta\mathcal{F}_M}}{Q}, Q \equiv \int \mathcal{D}\eta'(\mathbf{r}) e^{-\beta\mathcal{F}_M} \end{aligned}, \tag{3.19}$$

where $\mathcal{F}_M$ refers to the model free energy, $f_M[\eta(\mathbf{r})]$ is the quartic polynomial that represents the Landau-Ginzburg type Hamiltonian and $P_M[\eta(\mathbf{r})]$ is the probability distribution of $\eta(\mathbf{r})$ for a given $f(\eta)$ and κ. Atomistic simulations also yield observations of the field, which we denote as $\eta_i(\mathbf{r})$. Note that the simulation observations contain the subscript i or 'sim' and terms from the field theoretic model are subscripted with M. We can define the likelihood of observing these samples given the underlying model as,

$$\mathcal{L} = P_M[\eta_1(\mathbf{r})]P_M[\eta_2(\mathbf{r})]... = \prod_i P_M[\eta_i(\mathbf{r})]\,. \tag{3.20}$$

In order to maximise this likelihood (or equivalently, its logarithm), all the derivatives with respect to the model parameters must be zero. The corresponding solution set of $\{h, T_t, a, c, \kappa\}$ solutions yield the most optimal fit parameters. As an example, we show below this procedure for κ,

$$\begin{aligned} \frac{\partial \ln\mathcal{L}}{\partial\kappa} &= 0 = \sum_i \frac{\partial}{\partial\kappa}\ln P_M[\eta_i(\mathbf{r})] \\ &= \sum_i \frac{\partial}{\partial\kappa}\Big[-\beta\mathcal{F}_{\mathcal{M}} - \ln Q\Big] \\ &= \sum_i \frac{-\beta}{2}\Big[\int d\mathbf{r}|\nabla\eta_i|^2 - \Big\langle\int d\mathbf{r}|\nabla\eta(\mathbf{r})|^2\Big\rangle_M\Big]\,. \end{aligned}$$

Here $\langle|\nabla\eta(\mathbf{r})|^2\rangle_M$ is the average of this observable for the model with a given set of parameters. Also, $\sum_i \int d\mathbf{r}|\nabla\eta_i|^2 = N\big[|\nabla\eta_i|^2\big]_{\text{sim}}$ where N is the number of samples and the

averaging, denoted as [ ], is done over the simulation data. The above equations then simplify to,

$$\boxed{\Big[\int d\mathbf{r}|\nabla\eta_i|^2\Big]_{\text{sim}} = \Big\langle \int d\mathbf{r}|\nabla\eta(\mathbf{r})|^2\Big\rangle_M}. \tag{3.21}$$

Similarly for the other terms in the quartic polynomial with the power l, maximizing the likelihood means,

$$\boxed{\Big[\int d\mathbf{r}(\eta(\mathbf{r}))^l\Big]_{\text{sim}} = \Big\langle \int d\mathbf{r}(\eta(\mathbf{r}))^l\Big\rangle_M}. \tag{3.22}$$

Together, Eqs. 3.21 and 3.22 outline a new procedure to find the best set of field theory parameters that represent specific averages from the simulation data. For an initial set of $\{h, T_t, a, c, \kappa\}$, Monte Carlo simulations of the field theory could be performed to obtain model averages. Then, based on their difference from the simulation computed averages, gradient descent could be used to to adjust the parameters to find the $\{h, T_t, a, c, \kappa\}$ that maximize agreement with atomistic simulation averages. This maximum likelihood method will yield a field theoretic model that is very specific to the simulated system, which takes the simulation data into account, but lacks the generality and transparency of the mean-field approach we pursued.

Chapter 4

Free energy analysis and calculation of ligand properties

In Chap. 2 we described MD simulations of an atomistically detailed representation of ligands bound to a nanoparticle surface. This approach has the benefit of microscopic realism, but would be extremely costly to apply to systems comprising many nanoparticles. In Chap. 3 we presented a field theoretic model for ligand ordering. This cruder approach could easily be scaled up to treat systems of many nanoparticles, but its realism relies on choosing appropriate model parameters. In this chapter we close the loop of these complementary approaches. Specifically, we determine from MD simulations precisely the statistical quantities that are needed to construct a realistic field theory.

Central to these MD calculations is an ability to accurately determine thermodynamic biases governing fluctuations of the order parameter field. We therefore begin by describing the computation of free energy profiles along the ligand orientation parameter Θ_z.

4.1 Calculating free energy profiles for ligand ordering using multistate Bennett acceptance ratio method

The biased replica exchange MD simulations give access to the weights of different Θ_z values, which can be used to calculate the underlying free energy surface which the ligands explore. The Boltzmann weight of a given ligand configuration is related to the biased probability distribution of the order parameter obtained during the production run,

$$\begin{aligned} P_{\text{bias}}(r^N) &\propto e^{-\beta U_0(r^N)} e^{-\beta V_{\text{bias}}(r^N)} \\ \implies P_{\text{bias}}(r^N) &\propto p_0(r^N) e^{-\beta V_{\text{bias}}(r^N)} \,. \end{aligned}$$

Given the underlying equilibrium distribution $p_0(r^N)$, the likelihood of observing the probability described above is,

$$\mathcal{L} = \prod_{k=1}^{K} \prod_{n=1}^{N_k} P_{\text{bias}}(r_{kn}^N)\,, \tag{4.1}$$

where k is an index that runs over all the replicas K, n sums over the number of samples N_k collected for each replica k, $P_{\text{bias}}(r_{kn}^N) = p_0(r_{kn}^N)e^{-\beta V_k(r_{kn}^N)}$ is the observed probability and $Z_k = \sum_{n=1}^{N_k} P_{\text{bias}}(r_{kn}^N)$ is the partition function associated with the k^{th} replica. To maximize the likelihood of observing the given data with the underlying probability, we take the derivative of $\mathcal{L}$, or equivalently its logarithm, with respect to p_0 to get,

$$\frac{\partial \ln \mathcal{L}}{\partial p_0} = 0\,. \tag{4.2}$$

Simplifying Eq. 4.2 produces a set of self-consistent equation for the normalization weights $\{Z_k\}$ for each simulation, allowing one to reconstruct the underlying free energy landscape from the biased simulation data. This approach is known as the Multistate Bennett Acceptance Ratio (MBAR) method [4, 44] and it is advantageous compared to other techniques as it allows for calculation of free energies and thermal properties, while estimating errors in these quantities.

We used this method to obtain the free energy density as a function of the order parameter $\langle\theta_z\rangle$ at different temperatures in both vacuum and solvent. The Python package developed by Chodera and Shirts [44] was used to implement MBAR for the ligand biased replica exchange simulations. The free energy profiles in vacuum and hexane before and after the phase transition are shown in Figs. 4.1 and 4.2. The slope at the top of the barrier at a given temperature indicates the direction in which the system relaxes to find the global free energy minimum. As seen from Figs. 4.1 and 4.2, the sign of the slope changes as temperature increases, causing the ligands to disorder.

4.2 Interpolation of free energy to predict coexistence

We used the simulation data to interpolate between the sampled temperatures and calculate the temperature T_t at which the phase transition occurs. MBAR provides weights for different configurations at a given temperature and these can be re-weighted to different temperature by scaling the free energy by an appropriate factor. We then integrated the probability density,

$$p_{\langle\theta_z\rangle} \propto \exp\big(-\beta F(\langle\theta_z\rangle)\big)\,,$$

in each well representing the ordered and disordered phases to find the relative probability of being in one phase versus another, $p_{\text{rel}} = p_{\text{ord}}/p_{\text{disord}}$. The temperature at which $p_{\text{rel}} = 1$ is the coexistence temperature, where it is equally likely to find the system in either phase.

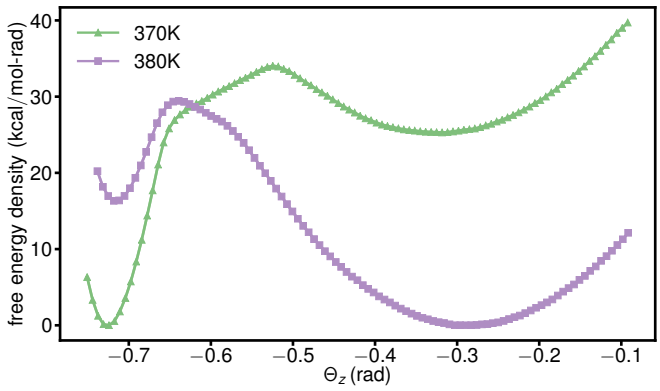

Figure 4.1: Free energy density in vacuum as a function of $\langle\theta_z\rangle$ at two different temperatures. The left-hand free energy minimum represents the ordered phase and the right-hand minimum is the disordered phase. As temperature increases, the global minimum switches from the ordered to disordered, showing that the system undergoes a first-order transition, similar to the schematic in Fig. 3.1.

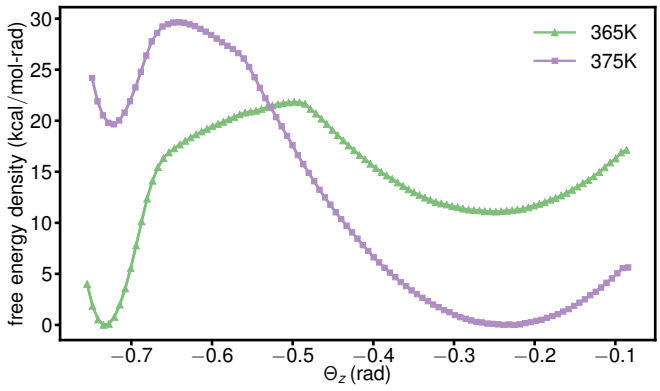

Figure 4.2: Free energy density in hexane solvent as a function of $\langle\theta_z\rangle$ at two different temperatures. The left-hand free energy minimum represents the ordered phase and the right-hand minimum is the disordered phase. As compared to Fig. 4.1, the temperatures are lower, showing that the phase transition occurs at a lower temperature.

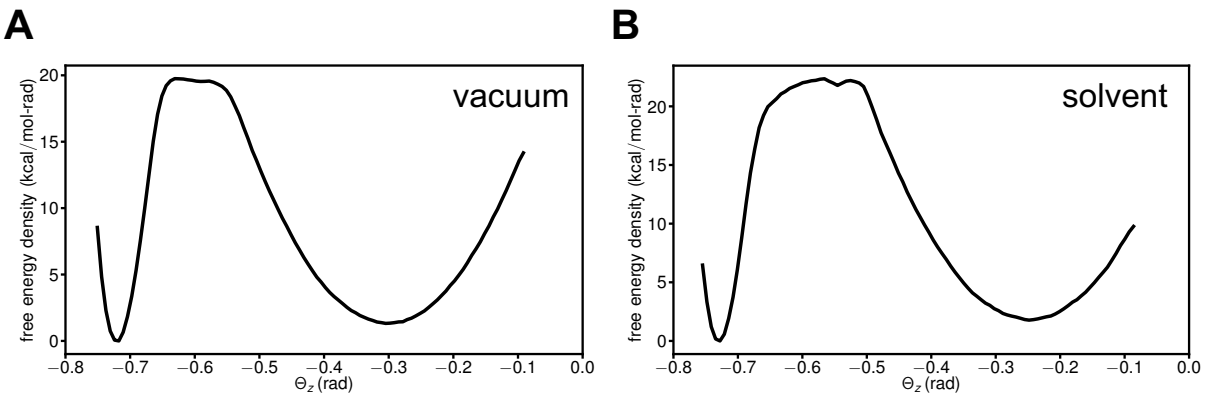

Figure 4.3: Free energy density in A) vacuum and B) hexane as a function of $\langle \theta_z \rangle$ at coexistence. These profiles are at different temperatures as the transition occurs at 375.6K in vacuum and 368.1K in solvent.

As determined by this method, the ligand ordering transition temperature in vacuum is $T_t = 375.6$K and in hexane is $T_t = 368.1$K. The corresponding free energy profiles at these coexistence temperatures in vacuum and solvent are shown below in Fig. 4.3. The slope at the top of the barrier is relatively flat in both vacuum and hexane, as compared to Figs. 4.1 and 4.2, indicating that the system is at coexistence.

4.3 Calculation of surface tension between ordered and disordered phases

Values of the order parameter Θ_z that lie between ranges typical of ordered and disordered phases are achieved in large systems by the development of an interface between ordered and disordered phases. The free energy profile at coexistence therefore quantifies the thermodynamic cost of creating such an interface, and can therefore be used to calculate surface tension σ.

For systems of modest size, such as the ligand layers we can study by MD simulation, the state of an interface at a given value of Θ_z is subject to uncertainty. For example, an intermediate value of the order parameter value could be achieved not only by introducing an interface, but also through a spontaneous fluctuation within one homogeneous phase. Furthermore, the shape of the interface at these scales may be very rough, and it may or may not connect through the simulation's periodic boundaries.

In order to extract a value of surface tension, we devised a simple model for decomposing the probability density into contributions from both uniform phases as well as interfacial configurations. The corresponding expression for the probability density is,

type	σ (kcal/mol-nm)
vacuum	1.28
solvent	1.42

Table 4.1: Surface tension values in vacuum as well as solvent obtained from the free energy profile at T_t.

$$P(\Theta) = P_{\rm ord}(\Theta, N) + P_{\rm disord}(\Theta, N) + P_{\rm int}(\Theta, \sigma)\,, \tag{4.3}$$

The first two terms in Eq.4.3 describe the probability of achieving the order parameter Θ within a single homogeneous phase, assuming Gaussian statistics within each phase. $P_{\rm ord}(\Theta, N)$ is thus a Gaussian centered at $\langle\theta_z\rangle_{\rm ord}$ with the appropriate variance in the ordered phase for N ligands. $P_{\rm disord}(\Theta)$ is a similar Gaussian for N ligands in the disordered phase centered at $\langle\theta_z\rangle_{\rm disord}$. The final term in Eq.4.3 describes the probability of achieving the value Θ in a state of coexistence. Considering all possible divisions of the system into ordered and disordered domains, we write $P_{\rm int}$ as,

$$P_{\rm int}(\Theta, \sigma) = \int_0^1 df\, \exp\left(-\beta\sigma L_z\right) \int_{-\infty}^{\infty} d\Theta_1 P_{\rm ord}(\Theta_1, fN) P_{\rm disord}\Big(\frac{\Theta - f\Theta_1}{1-f}, (1-f)N\Big)\,. \tag{4.4}$$

Here, f denotes the fraction of ligands in this heterogeneous system that reside in the ordered phase; the remaining fraction $(1-f)$ reside in the disordered phase. We have assumed that the interface spans the length of the CdS surface in the $z-$ direction (as observed in simulations, see Fig. 2.10).

We fit the free energy profile at coexistence to the probability distribution proposed in Eq. 4.3 to obtain the optimal value of σ that best described the cost of forming an interface. The best-fit free energy profiles in vacuum and hexane are shown in Fig. 4.4. The corresponding values of σ are given in Table 4.1.

4.4 Entropy change due to phase transition

To calculate the entropy difference between the ordered and disordered phase, we use the thermodynamic relation,

$$\Delta S = \frac{\Delta E - \Delta F}{T} \tag{4.5}$$

The MD simulations track the ligand energies, and these can be binned at each Θ_z value to obtain, $E(\Theta_z)$, as shown in Fig. 4.5 A (for ligands in vacuum) and B (ligands in solvent). Integrating over order parameter ranges corresponding to ordered and disordered phases, the energy of each phase can be calculated as,

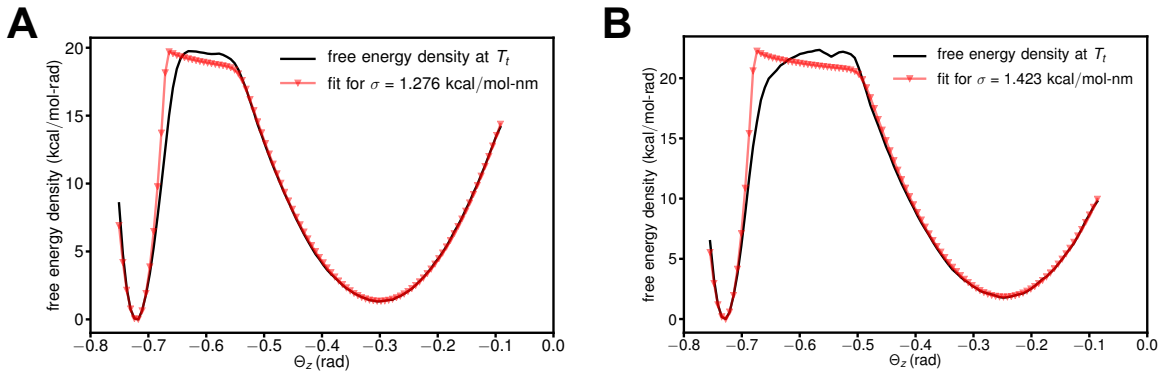

Figure 4.4: Fit to the free energy profile at coexistence to calculate the value of surface tension σ in A) vacuum and B) solvent. The black line shows the free energy at T_t obtained using MBAR and the red is the fit in Eq. 4.3.

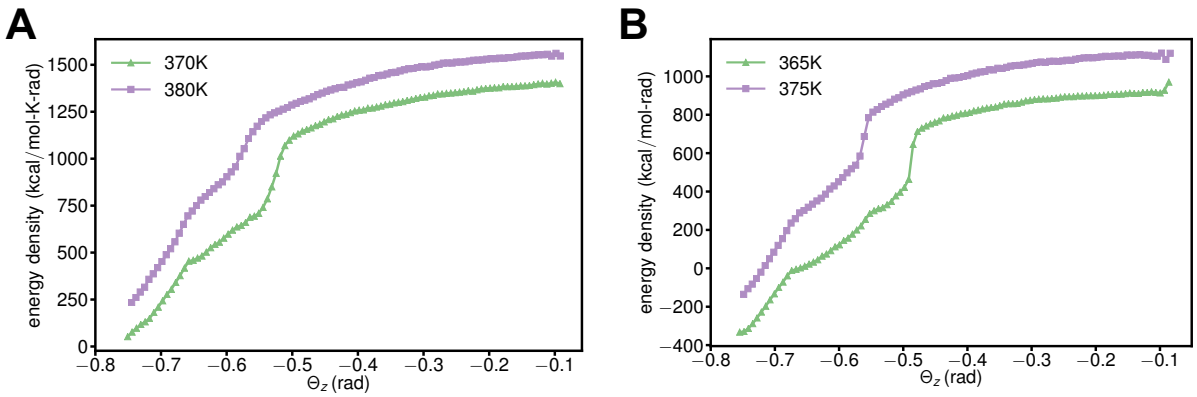

Figure 4.5: Variation of ligand energy with respect to $\langle\theta_z\rangle$ in A) vacuum and B) solvent. Energy values were obtained during MBAR simulations and binned along the order parameter axis at different temperatures. The jump in the energy tracks the disordering of the ligand molecules.

$$E_{\mathrm{X}} = \int_{-\infty}^{\infty} d\Theta\, P_{\mathrm{X}}(\Theta) e(\Theta)\,, \tag{4.6}$$

where E_{X} is the energy of phase X and $e(\Theta)$ is the energy density for configurations with an order parameter value Θ. The energy difference is then given by,

$$\Delta E = E_{\mathrm{disord}} - E_{\mathrm{ord}}\,. \tag{4.7}$$

Temperature (K)	ΔS (kcal/mol-K)
370	1.27
380	1.47
375.6	1.38

Table 4.2: Entropy difference between the ordered and disordered phases in vacuum.

Temperature (K)	ΔS (kcal/mol-K)
365	0.90
375	1.12
368	0.97

Table 4.3: Entropy difference between the ordered and disordered phases in hexane.

The corresponding free energy difference is given by integrating probability density in each phase,

$$\Delta F = F_{\text{disord}} - F_{\text{ord}} = -k_B \ln\left(\frac{Q_{\text{disord}}}{Q_{\text{ord}}}\right), \tag{4.8}$$

where $Q_{\text{X}} \propto \int_{-\infty}^{\infty} d\Theta\, P_{\text{X}}(\Theta)$. Plugging these back into Eq. 4.5, we obtained the entropy difference between the two phases at several temperatures in both vacuum and solvent. ΔS was linearly interpolated to estimate the entropy difference at T_t. The resulting values are shown in Tables 4.2 and 4.3.

4.5 Spatial correlation decay length calculations

The spatial correlation decay length for both phases was calculated by analyzing the correlation functions for the $\langle \phi_z \rangle$ order parameter, which are plotted in Figs. 2.17 and 2.22. As derived in Eq. 3.18, the expected functional form of $G_\phi(r)$ is a zeroth order modified Bessel of the second kind. We fit the correlation functions to $K_0(r/\lambda)$ to obtain the decay length. For the disordered phase, $G_\phi(z)$ was used for this purpose but not $G_\phi(x)$; as described in Chap. 2, correlations in the $x-$direction exhibit oscillations in the disordered phase, originating in fine structural patterns that lie outside the scope of our field theory. The fits for both phases are shown in Figs. 4.6 and 4.7, for vacuum and solvent respectively. The associated decay lengths are given in Tables 4.4 and 4.5. The average between the two phases was used as the λ value in the field theory.

Phase	λ (nm)
ordered	0.90
disordered	1.10

Table 4.4: Spatial correlation decay lengths in vacuum for both ligand phases.

Phase	λ (nm)
ordered	1.44
disordered	1.56

Table 4.5: Spatial correlation decay lengths in solvent for both ligand phases.

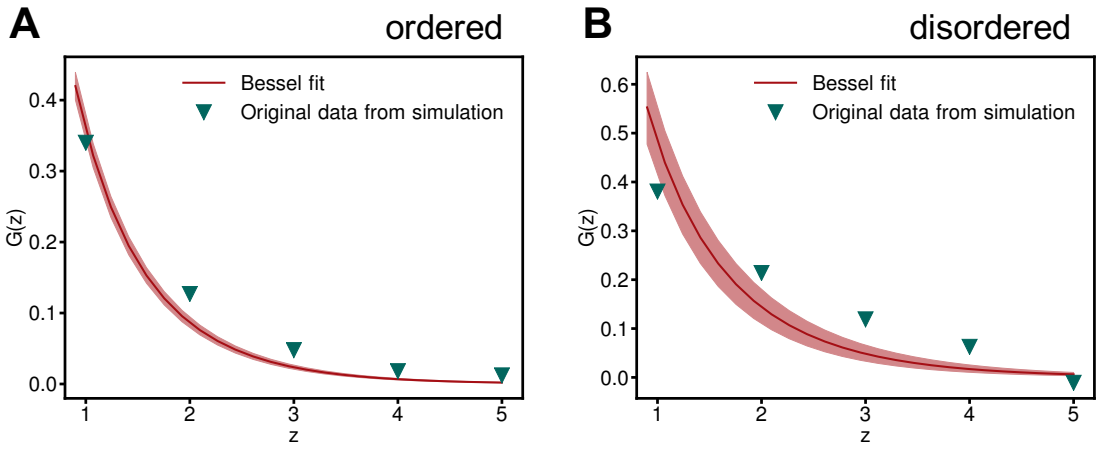

Figure 4.6: Modified Bessel function fits to the spatial correlation G_ϕ along the z-direction in vacuum. A) shows the fit for the ordered phase and B) is the corresponding fit in the disordered phase. The shaded region around the fit depicts the error in the fit parameters.

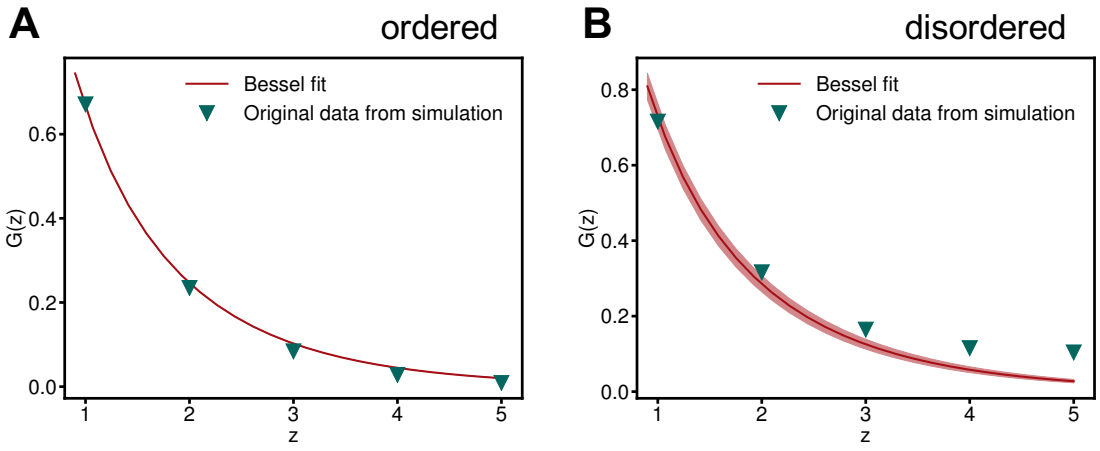

Figure 4.7: Spatial correlation G_ϕ along the z-direction in solvent fitted with a modified Bessel function with A) showing the fit for the ordered phase and B) in the disordered phase. The shaded region represents the uncertainty of the fit.

Medium	$\langle\theta_z\rangle_{\text{ord}}$ (rad)	$\langle\theta_z\rangle_{\text{disord}}$ (rad)	$\Delta\langle\theta_z\rangle$ (rad)
vacuum	-0.72	-0.30	0.42
hexane	-0.73	-0.25	0.48

Table 4.6: Order parameter values where free energy is minimized, showing the thermal averages, $\langle\theta_z\rangle$, for the ordered and disordered phases, both in vacuum and solvent.

4.6 Difference between order parameter minima

We interpolated the free energy to multiple temperatures using MBAR to track how the $\langle\theta_z\rangle$ values change with temperature. We found that $\langle\theta_z\rangle_{\text{ord}}$ and $\langle\theta_z\rangle_{\text{disord}}$ do not change significantly over the temperature range of interest in both vacuum and solvent, and hence, $\Delta\langle\theta_z\rangle$ can be taken to be constant. Fig. 4.8 shows the behavior of $\langle\theta_z\rangle_{\text{ord}}$, $\langle\theta_z\rangle_{\text{disord}}$ and $\Delta\langle\theta_z\rangle$ as a function of temperature in vacuum and in hexane. The resulting difference for both vacuum and solvent at their respective transition temperatures is given in Table 4.6.

4.7 Calculated field theory parameters in vacuum and solvent

With all the physical properties of the ligands obtained from MD simulations, we were able to parameterize our field theoretic model (Eq. 3.5). The resulting values of $\{h, T_t, a, c, \kappa\}$

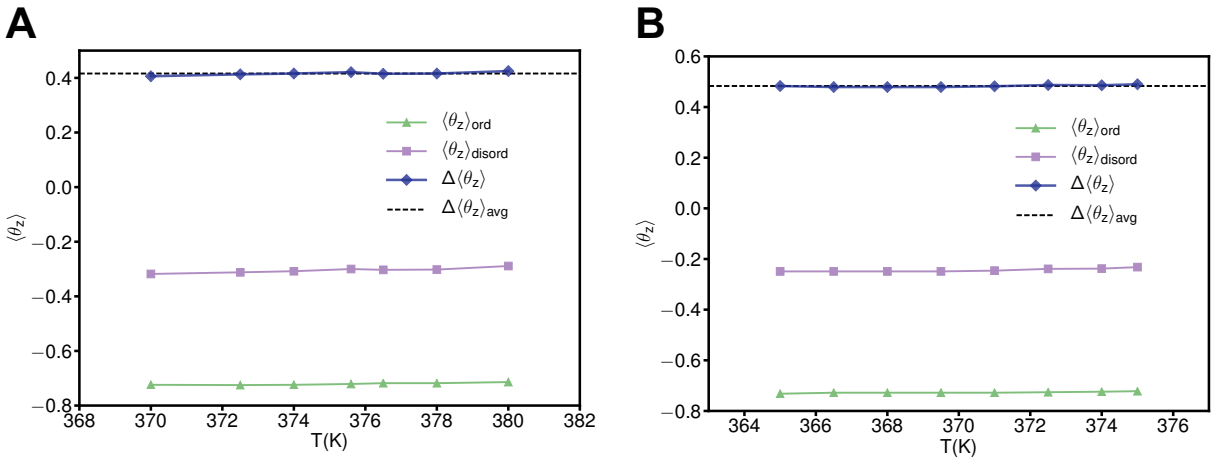

Figure 4.8: A) The variation of $\langle\theta_z\rangle_{\rm ord}$ (in green), $\langle\theta_z\rangle_{\rm disord}$ (in purple) and $\Delta\langle\theta_z\rangle$ (in blue) in vacuum as a function of temperature. $\Delta\langle\theta_z\rangle$ does not vary much with temperature and can be taken to be the average value. B) The same quantities are plotted in hexane.

Parameter	Value
h	-0.0492 kcal/mol-K-rad
T_t	375.6K
a	-31.9 kcal/mol-nm-rad^2
c	720.0 kcal/mol-nm-rad^4
κ	31.8 kcal/mol-nm^2

Table 4.7: The values of the field theoretic model parameters in vacuum, obtained by solving Eqs. 3.9, 3.10, 3.15 and 3.19 with properties calculated from the free energy profiles.

are given in Tables 4.7 (for ligands in vacuum) and 4.8 (for ligands in hexane solvent).

Using these parameters, the field theoretic homogeneous free energy density $f(\eta)$ can be computed for the order parameter $\eta = \Theta - (\langle\theta_z\rangle_{\rm disord} + \langle\theta_z\rangle_{\rm ord})/2$ These free energy profiles are shown in Figs. 4.9 (vacuum) and 4.10 (hexane) for temperatures spanning the ordering transition. The barriers between ordered and disordered wells in these plots are considerably lower than those in free energy profiles computed from MD simulations. Caution should be used, however, in making this comparison.

Firstly, the homogeneous free energy density $f(\eta)$ is intended exclusively to describe single-phase systems, and not to capture scenarios of coexistence. The barrier in $f(\eta)$ is certainly significant for interfacial physics, as it encourages sharp surfaces that minimize excursions of the local order parameter away from values characteristic of the stable ordered

Parameter	Value
h	-0.0301 kcal/mol-K-rad
T_t	368.0K
a	-18.9 kcal/mol-nm-rad^2
c	324.0 kcal/mol-nm-rad^4
κ	42.6 kcal/mol-nm^2

Table 4.8: The values of the coarse-grained model parameters in hexane, obtained by solving Eqs. 3.9, 3.10, 3.15 and 3.19 using the properties calculated from the MD simulation data analysis.

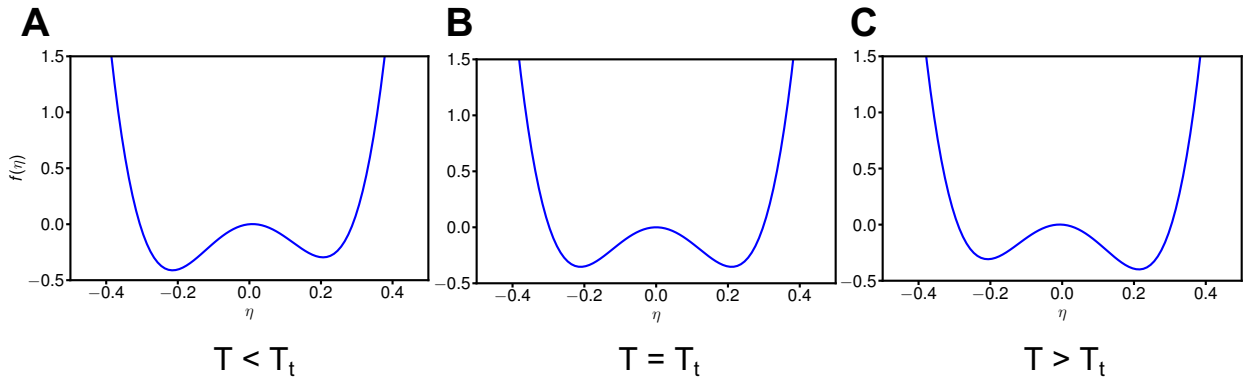

Figure 4.9: Variation of the local free energy $f(eta)$ using the model parameters in 4.7 for vacuum at A) a temperature below T_t, B) the transition temperature and C) a temperature above T_t. The mean-field theory assumptions lead to a lower free energy barrier between the two phases as compared to the free energy profiles calculated from MD simulations, in Fig. 4.1.

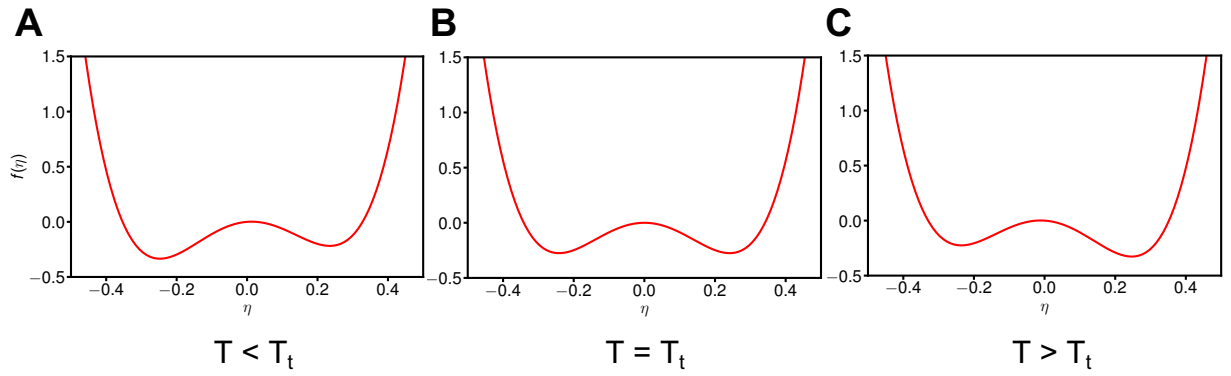

Figure 4.10: The local free energy $f(\eta)$ plotted using the model parameters in 4.8 in solvent at A) $T < T_t$, B) T_t and C) $T > T_t$. The mean-field theory assumptions lead to a lower free energy barrier between the two phases as compared to the free energy profiles shown in Fig. 4.2.

and disordered phases. But it is only one factor affecting the surface tension. As emphasized by Eq.3.14, the square gradient coefficient κ counteracts the influence of the barrier in $f(\eta)$, instead discouraging rapid spatial variations of the order parameter.

Secondly, our field theoretic analysis rests on the saddle point approximation, whereas MD simulations clearly describe a fully fluctuating model. Our intent to capture the essence of the ligand ordering transition with mean field theory can succeed even while detailed comparison of its ingredients appear unfavorable. In other words, we have parameterized a mean field model to be faithful to observed features of the ligand ordering transition. So parameterized, the fully fluctuating counterpart of this field theory might well be less realistic.

Indeed, the full field theory of Chap. 3, when parameterized according to its mean field behavior, does not mimic well the ligand behavior observed in MD simulations. We performed Monte Carlo simulations of the fully fluctuating nonlinear field theory of Eq. 3.5 with the parameters given in Tables 4.7 and 4.8. We used a square lattice, with fluctuating values of Θ at each grid point. The Metropolis-Hastings criterion was used to perform moves that changed each grid point's order parameter value and statistics were collected to obtain $\langle\theta_z\rangle$ as a function of temperature. Results, shown in Fig. 4.11 for vacuum and hexane, are not consistent with a first-order phase transition, as there is not sharp transition in the order parameter value at T_t. Instead, there is a steady increase in $\langle\theta_z\rangle$ with temperature, and the system explores both positive and negative $\langle\theta_z\rangle$ during the course of the simulation. Because the barrier in $f(\eta)$ is low, and the fitted value of κ is modest, fluctuations that are neglected in mean field theory disrupt symmetry breaking, and the phase transition does not survive.

As one test of this understanding, we increased the value of κ by an order of magnitude, to $\kappa_{\text{high}} = 318\,\text{kcal/mol-nm}^2$, while keeping the other parameters the same as in Table

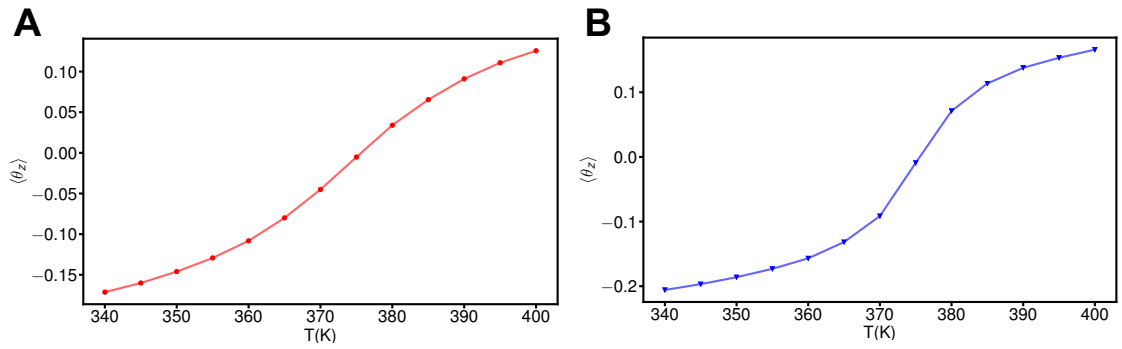

Figure 4.11: The variation of $\langle\theta_z\rangle$ with temperature, obtained from performing the MC simulations of the coarse-grained model. A) shows the behavior of the order parameter in solvent and B) is the same, in hexane. These plots are not characteristic of a first-order phase transition as there is not sudden jump in the order parameter value at T_t. This is due to the mean-field assumptions made in order to derive the equations for the model parameters.

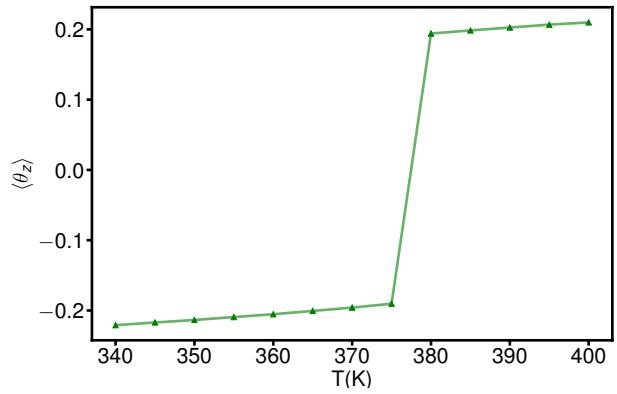

Figure 4.12: $\langle\theta_z\rangle$ plotted as a function of temperature with a κ_{new} value an order of magnitude higher than given in 4.7 for vacuum. This behavior is what we expect for a first-order phase transition, indicating that the assumptions made to calculate the model parameters result in a κ value that is too small with respect to $k_{\text{B}}T$ in the temperature range sampled.

4.7. Monte Carlo simulations for this case yielded the much more abruptly varying order parameter profile shown in Fig. 4.12. By suppressing fluctuations, the phase transition is recovered.

We conclude that internal consistency is crucial in parameterizing and deploying such a coarse-grained field theory. The mean field approach we have followed offers a fairly simple route forwards for developing a reduced description of more complex systems, in which for instance the ligand layers of numerous nanoparticle influence one another's ordering

tendencies. But it necessarily suffers from the underlying neglect of fluctuations. While these fluctuations could play an important role when multiple ligand layers interact or when the finite sizes of nanoparticle facets are significant, the lack of a nearby critical point suggests they will generally be inessential.

In order to examine the effects of fluctuations in a full nonlinear field theory for interacting ligand layers, one should begin by parameterizing the theory in a consistent way – without appealing to mean field theory. The maximum likelihood method sketched in Section 3.3 offers one way to accomplish this parameterization. At each stage, however, it would be necessary to account for fluctuations. Extending the theory to address edge effects or the interactions of multiple layers could become very complicated as a result.

Bibliography

[1] A. P. Alivisatos. "Semiconductor Clusters, Nanocrystals, and Quantum Dots". English. In: *Science* 271.5251 (Feb. 1996), p. 933. ISSN: 00368075.

[2] Jessy L. Baker et al. "Device-Scale Perpendicular Alignment of Colloidal Nanorods". In: *Nano Lett.* 10.1 (Jan. 2010), pp. 195–201. ISSN: 1530-6984. DOI: 10.1021/nl903187v.

[3] Arunima D. Balan et al. "Unsaturated Ligands Seed an Order to Disorder Transition in Mixed Ligand Shells of CdSe/CdS Quantum Dots". In: *ACS Nano* (Nov. 2019). ISSN: 1936-0851. DOI: 10.1021/acsnano.9b03054.

[4] Charles H Bennett. "Efficient Estimation of Free Energy Differences from Monte Carlo Data". en. In: *J. Comput. Phys.* 22.2 (Oct. 1976), pp. 245–268. ISSN: 0021-9991. DOI: 10.1016/0021-9991(76)90078-4.

[5] Michael A. Boles and Dmitri V. Talapin. "Binary Assembly of PbS and Au Nanocrystals: Patchy PbS Surface Ligand Coverage Stabilizes the CuAu Superlattice". In: *ACS Nano* 13.5 (May 2019), pp. 5375–5384. ISSN: 1936-0851. DOI: 10.1021/acsnano.9b00006.

[6] Giovanni Bussi and Gareth A. Tribello. "Analyzing and Biasing Simulations with PLUMED". en. In: *Biomolecular Simulations: Methods and Protocols*. Ed. by Massimiliano Bonomi and Carlo Camilloni. Methods in Molecular Biology. New York, NY: Springer, 2019, pp. 529–578. ISBN: 978-1-4939-9608-7. DOI: 10.1007/978-1-4939-9608-7_21.

[7] Hans-Jürgen Butt and Michael Kappl. *Surface and Interfacial Forces*. 2nd ed. Germany: John Wiley & Sons, Ltd, 2010. DOI: 10.1002/9783527804351.

[8] Ronny Costi, Aaron E. Saunders, and Uri Banin. "Colloidal Hybrid Nanostructures: A New Type of Functional Materials". In: *Angew. Chem. Int. Edit.* 49.29 (July 2010), pp. 4878–4897. ISSN: 1433-7851. DOI: 10.1002/anie.200906010.

[9] S. Doniach. "Thermodynamic Fluctuations in Phospholipid Bilayers". In: *J. Chem. Phys.* 68.11 (June 1978), pp. 4912–4916. ISSN: 0021-9606. DOI: 10.1063/1.435647.

[10] Fabien Dubois et al. "A Versatile Strategy for Quantum Dot Ligand Exchange". In: *J. Am. Chem. Soc.* 129.3 (Jan. 2007), pp. 482–483. ISSN: 0002-7863. DOI: 10.1021/ja067742y.

[11] Zhaochuan Fan and Michael Grünwald. "Orientational Order in Self-Assembled Nanocrystal Superlattices". In: *J. Am. Chem. Soc.* 141.5 (Feb. 2019), pp. 1980–1988. ISSN: 0002-7863. DOI: 10.1021/jacs.8b10752.

[12] Pradip Kr. Ghorai and Sharon C. Glotzer. "Molecular Dynamics Simulation Study of Self-Assembled Monolayers of Alkanethiol Surfactants on Spherical Gold Nanoparticles †". en. In: *J. Phys. Chem. C* 111.43 (Nov. 2007), pp. 15857–15862. ISSN: 1932-7447, 1932-7455. DOI: 10.1021/jp0746289.

[13] V. L. Ginzburg and L. D. Landau. "On the Theory of Superconductivity". en. In: *On Superconductivity and Superfluidity: A Scientific Autobiography*. Ed. by Vitaly L. Ginzburg. Berlin, Heidelberg: Springer, 2009, pp. 113–137. ISBN: 978-3-540-68008-6. DOI: 10.1007/978-3-540-68008-6_4.

[14] Vitaly Lazarevich Ginzburg and Lev Davidovich Landau. "On the Theory of Superconductivity". In: *Zh. Eksp. Teor. Fiz.* 20 (1950).

[15] Martin Hasenbusch and Stefan Schaefer. "Speeding up Parallel Tempering Simulations". In: *Phys. Rev. E* 82.4 (Oct. 2010), p. 046707. DOI: 10.1103/PhysRevE.82.046707.

[16] Yasitha L. Hewakuruppu et al. "Plasmonic “Pump–Probe” Method to Study Semi-Transparent Nanofluids". EN. In: *Appl. Optics* 52.24 (Aug. 2013), pp. 6041–6050. ISSN: 2155-3165. DOI: 10.1364/AO.52.006041.

[17] Robert J. Hickey et al. "Directional Self-Assembly of Ligand-Stabilized Gold Nanoparticles into Hollow Vesicles through Dynamic Ligand Rearrangement". In: *Langmuir* 31.14 (Apr. 2015), pp. 4299–4304. ISSN: 0743-7463. DOI: 10.1021/la503903n.

[18] P. C. Hohenberg and A. P. Krekhov. "An Introduction to the Ginzburg-Landau Theory of Phase Transitions and Nonequilibrium Patterns". In: *Phys. Rep.* 572 (Apr. 2015), pp. 1–42. ISSN: 03701573. DOI: 10.1016/j.physrep.2015.01.001. arXiv: 1410.7285.

[19] Jing Huang, Maksym V. Kovalenko, and Dmitri V. Talapin. "Alkyl Chains of Surface Ligands Affect Polytypism of CdSe Nanocrystals and Play an Important Role in the Synthesis of Anisotropic Nanoheterostructures". In: *J. Am. Chem. Soc.* 132.45 (Nov. 2010), pp. 15866–15868. ISSN: 0002-7863. DOI: 10.1021/ja105132u.

[20] Wendy U. Huynh, Janke J. Dittmer, and A. Paul Alivisatos. "Hybrid Nanorod-Polymer Solar Cells". en. In: *Science* 295.5564 (Mar. 2002), pp. 2425–2427. ISSN: 0036-8075, 1095-9203. DOI: 10.1126/science.1069156.

[21] Alicia M. Jackson et al. "From Homoligand- to Mixed-Ligand- Monolayer-Protected Metal Nanoparticles: A Scanning Tunneling Microscopy Investigation". In: *J. Am. Chem. Soc.* 128.34 (Aug. 2006), pp. 11135–11149. ISSN: 0002-7863. DOI: 10.1021/ja061545h.

[22] Blanka E. Janicek et al. "Quantitative Imaging of Organic Ligand Density on Anisotropic Inorganic Nanocrystals". In: *Nano Lett.* 19.9 (Sept. 2019), pp. 6308–6314. ISSN: 1530-6984. DOI: 10.1021/acs.nanolett.9b02434.

[23] Zachary C. Kennedy et al. "Influence of Ligand Shell Composition upon Interparticle Interactions in Multifunctional Nanoparticles". en. In: *Langmuir* 31.46 (Nov. 2015), pp. 12742–12752. ISSN: 0743-7463, 1520-5827. DOI: 10.1021/acs.langmuir.5b03096.

[24] Lev Davidovich Landau. "On the Theory of Phase Transitions". In: *Zh. Eksp. Teor. Fiz.* 7 (1937), pp. 19–32.

[25] David R. Lide. *CRC Handbook of Chemistry and Physics*. 86th ed. Boca Raton, FL: CRC Press, Taylor & Francis, 2005. DOI: 10.1021/ja059868l.

[26] David T. Limmer and David Chandler. "Phase Diagram of Supercooled Water Confined to Hydrophilic Nanopores". In: *J. Chem. Phys.* 137.4 (July 2012), p. 044509. ISSN: 0021-9606. DOI: 10.1063/1.4737907.

[27] David T. Limmer and David Chandler. "Premelting, Fluctuations, and Coarse-Graining of Water-Ice Interfaces". In: *J. Chem. Phys.* 141.18 (Sept. 2014), p. 18C505. ISSN: 0021-9606. DOI: 10.1063/1.4895399.

[28] Marcus G. Martin and J. Ilja Siepmann. "Transferable Potentials for Phase Equilibria. 1. United-Atom Description of n-Alkanes". In: *J. Phys. Chem. B* 102.14 (Apr. 1998), pp. 2569–2577. ISSN: 1520-6106. DOI: 10.1021/jp972543+.

[29] Andrea D. Merg et al. "Ligand Exchange for Controlling the Surface Chemistry and Properties of Nanoparticle Superstructures". en. In: *ChemNanoMat* 3.10 (2017), pp. 745–749. ISSN: 2199-692X. DOI: 10.1002/cnma.201700171.

[30] Miguel A. Modestino et al. "Controlling Nanorod Self-Assembly in Polymer Thin Films". In: *Macromolecules* 44.18 (Sept. 2011), pp. 7364–7371. ISSN: 0024-9297. DOI: 10.1021/ma201252d.

[31] O. G. Mouritsen et al. "Computer Simulation of the Main Gel–Fluid Phase Transition of Lipid Bilayers". In: *J. Chem. Phys.* 79.4 (Aug. 1983), pp. 2027–2041. ISSN: 0021-9606. DOI: 10.1063/1.445987.

[32] C. B. Murray, C. R. Kagan, and M. G. Bawendi. "Synthesis and Characterization of Monodisperse Nanocrystals and Close-Packed Nanocrystal Assemblies". In: *Annu. Rev. Mater. Sci.* 30.1 (Aug. 2000), pp. 545–610. ISSN: 0084-6600. DOI: 10.1146/annurev.matsci.30.1.545.

[33] Shyamal K. Nath, Fernando A. Escobedo, and Juan J. de Pablo. "On the Simulation of Vapor–Liquid Equilibria for Alkanes". In: *J. Chem. Phys.* 108.23 (June 1998), pp. 9905–9911. ISSN: 0021-9606. DOI: 10.1063/1.476429.

[34] Marie-Alexandra Neouze and Ulrich Schubert. "Surface Modification and Functionalization of Metal and Metal Oxide Nanoparticles by Organic Ligands". en. In: *Monatsh Chem.* 139.3 (Mar. 2008), pp. 183–195. ISSN: 1434-4475. DOI: 10.1007/s00706-007-0775-2.

[35] Justin C. Ondry et al. "Resilient Pathways to Atomic Attachment of Quantum Dot Dimers and Artificial Solids from Faceted CdSe Quantum Dot Building Blocks". In: *ACS Nano* 13.11 (Nov. 2019), pp. 12322–12344. ISSN: 1936-0851. DOI: 10.1021/acsnano.9b03052.

[36] Xiaogang Peng et al. "Shape Control of CdSe Nanocrystals". English. In: *Nature* 404.6773 (Mar. 2000), pp. 59–61. ISSN: 00280836. DOI: http://dx.doi.org/10.1038/35003535.

[37] Steve Plimpton. "Fast Parallel Algorithms for Short-Range Molecular Dynamics". en. In: *J. Comput. Phys.* 117.1 (Mar. 1995), pp. 1–19. ISSN: 0021-9991. DOI: 10.1006/jcph.1995.1039.

[38] Paul Podsiadlo et al. "The Role of Order, Nanocrystal Size, and Capping Ligands in the Collective Mechanical Response of Three-Dimensional Nanocrystal Solids". In: *J. Am. Chem. Soc.* 132.26 (July 2010), pp. 8953–8960. ISSN: 0002-7863. DOI: 10.1021/ja100464a.

[39] René Pool, Philipp Schapotschnikow, and Thijs J. H. Vlugt. "Solvent Effects in the Adsorption of Alkyl Thiols on Gold Structures: A Molecular Simulation Study". In: *J. Phys. Chem. C* 111.28 (July 2007), pp. 10201–10212. ISSN: 1932-7447. DOI: 10.1021/jp071491d.

[40] Aurora Rizzo et al. "Polarized Light Emitting Diode by Long-Range Nanorod Self-Assembling on a Water Surface". In: *ACS Nano* 3.6 (June 2009), pp. 1506–1512. ISSN: 1936-0851. DOI: 10.1021/nn900063m.

[41] Sandra J. Rosenthal et al. "Synthesis, Surface Studies, Composition and Structural Characterization of CdSe, Core/Shell and Biologically Active Nanocrystals". en. In: *Surf. Sci. Rep.* 62.4 (Apr. 2007), pp. 111–157. ISSN: 0167-5729. DOI: 10.1016/j.surfrep.2007.02.001.

[42] Aaron Santos, Jaime Andres Millan, and Sharon C. Glotzer. "Facetted Patchy Particles through Entropy-Driven Patterning of Mixed Ligand SAMS". en. In: *Nanoscale* 4.8 (Mar. 2012), pp. 2640–2650. ISSN: 2040-3372. DOI: 10.1039/C2NR11737A.

[43] P. E. Sheehan et al. "Nanoscale Deposition of Solid Inks via Thermal Dip Pen Nanolithography". In: *Appl. Phys. Lett.* 85.9 (Aug. 2004), pp. 1589–1591. ISSN: 0003-6951. DOI: 10.1063/1.1785860.

[44] Michael R. Shirts and John D. Chodera. "Statistically Optimal Analysis of Samples from Multiple Equilibrium States". In: *J. Chem. Phys.* 129.12 (Sept. 2008), p. 124105. ISSN: 0021-9606. DOI: 10.1063/1.2978177.

[45] Yuji Sugita, Akio Kitao, and Yuko Okamoto. "Multidimensional Replica-Exchange Method for Free-Energy Calculations". en. In: *J. Chem. Phys.* 113.15 (Oct. 2000), pp. 6042–6051. ISSN: 0021-9606, 1089-7690. DOI: 10.1063/1.1308516.

[46] Andrea R. Tao, Susan Habas, and Peidong Yang. "Shape Control of Colloidal Metal Nanocrystals". en. In: *Small* 4.3 (2008), pp. 310–325. ISSN: 1613-6829. DOI: 10.1002/smll.200701295.

[47] Thibaut Thai et al. "Self-Assembly of Vertically Aligned Gold Nanorod Arrays on Patterned Substrates". In: *Angew. Chem. Int. Ed.* 51.35 (2012), pp. 8732–8735. ISSN: 1521-3773. DOI: 10.1002/anie.201204609.

[48] Asaph Widmer-Cooper and Phillip Geissler. "Orientational Ordering of Passivating Ligands on CdS Nanorods in Solution Generates Strong Rod–Rod Interactions". In: *Nano Lett.* 14.1 (Jan. 2014), pp. 57–65. ISSN: 1530-6984. DOI: 10.1021/nl403067p.

[49] Asaph Widmer-Cooper and Phillip L. Geissler. "Ligand-Mediated Interactions between Nanoscale Surfaces Depend Sensitively and Nonlinearly on Temperature, Facet Dimensions, and Ligand Coverage". In: *ACS Nano* 10.2 (Feb. 2016), pp. 1877–1887. ISSN: 1936-0851. DOI: 10.1021/acsnano.5b05569.

[50] Meng Wu et al. "Solution NMR Analysis of Ligand Environment in Quaternary Ammonium-Terminated Self-Assembled Monolayers on Gold Nanoparticles: The Effect of Surface Curvature and Ligand Structure". In: *J. Am. Chem. Soc.* 141.10 (Mar. 2019), pp. 4316–4327. ISSN: 0002-7863. DOI: 10.1021/jacs.8b11445.

[51] Zhikun Wu and Rongchao Jin. "On the Ligand's Role in the Fluorescence of Gold Nanoclusters". In: *Nano Lett.* 10.7 (July 2010), pp. 2568–2573. ISSN: 1530-6984. DOI: 10.1021/nl101225f.

[52] Yue Zhao et al. "Small-Molecule-Directed Nanoparticle Assembly towards Stimuli-Responsive Nanocomposites". en. In: *Nat. Mater.* 8.12 (Dec. 2009), pp. 979–985. ISSN: 1476-4660. DOI: 10.1038/nmat2565.